Supporting Information

$[Ag_{62}S_{12}(CBT)_{32}]^{4+}$: A 2.2 nm Two-Electron Superatomic Carborane-Thiolated Silver Nanocluster Exhibiting Multilayer Charge Separation

Arijit Jana,[a] Vivek Yadav,[a] Monika Kučeráková,[b] Sami Malola,[c] Amoghavarsha Ramachandra Kini,[a] Swetashree Acharya,[a] Ajay K. Poonia,[d] Jan Macháček,[e] Kumaran Nair Valsala Devi Adarsh,*[d] Hannu Häkkinen,*[c] Tomas Base,*[e] and Thalappil Pradeep*[a]

[a] DST Unit of Nanoscience (DST UNS) and Thematic Unit of Excellence (TUE), Department of Chemistry, Indian Institute of Technology, Madras, Chennai – 600036, India

[b] Department of Structure Analysis, Institute of Physics, The Czech Academy of Sciences, Na Slovance 2, 182 21 Prague 8, Czech Republic

[c] Departments of Physics and Chemistry, Nanoscience Center, University of Jyväskylä, FI 40014 Jyväskylä, Finland

[d] Department of Physics, Indian Institute of Science Education and Research Bhopal, Bhopal – 462066, India

[e] Department of Syntheses, Institute of Inorganic Chemistry, The Czech Academy of Sciences, 250 68 Husinec-Řež, č.p. 1001, Czech Republic

* Email: *pradeep@iitm.ac.in, tbase@iic.cas.cz, hannu.j.hakkinen@jyu.fi, adarsh@iiserb.ac.in*

Table of content:

Instrumentation

Optical microscopy: Optical microscopic images of the crystals were collected in transmission mode using a LEICA optical microscope equipped with LAS V4.8 software.

Scanning Electron microscopy: Scanning electron microscopic (SEM) images are recorded using Verios G4 UC, Thermo Scientific field emission scanning electron microscope (FESEM). After transferring the crystal on a carbon tape, gold sputtering (2 min) was performed to increase the conductivity. FESEM images were collected in high vacuum at an operating voltage of 10-15 kV.

UV-vis absorption spectroscopy: UV-vis absorption spectra were measured in transmission mode using Perkin Elmer Lambda 365 UV-vis spectrometer using a bandpass filter of 1 nm. **Photoluminescence spectroscopy:** Photoluminescence spectra were measured using a Jobin Yvon Nanolog fluorescence spectrometer using a slit width of 3 nm and a resolution bandwidth of 5 nm. The Nanolog instrument has a 450 W xenon-arc lamp source, double monochromator with kinetic gratings, associated reflective optics, and CCD detector. Cluster were dissolved in DMF (2.5 ml) was placed in a 1 cm quartz cuvette to measure the spectrum.

Mass spectrometry: Mass spectra of the cluster was measured using Waters Synapt G2Si HDMS instrument. The instrument is equipped with an electrospray ionization source, mass selected ion trap, ion mobility cells, and time of flight mass analyzer. An optimized operating conditions such as flow rate 20 μL/min, capillary voltage 2.5 kV, cone voltage 20 V, source offset 10 V, desolvation gas flow 400 L/min and source temperature 80-100 °C were used for the measurements. Collision-induced dissociation (CID) studies were performed upon colliding the selected molecular ion with argon gas inside the trap cell of the instrument. Gradually increasing the collision energy (CE 0 to 70 for Ag_{62}) leads to the fragmentation of the species. All the measurements used low concentration (~ 1 μg/ml) of cluster sample.

Infrared spectroscopy: FT-IR spectra were measured using a JASCO-4100 FT-IR spectrometer after preparing potassium bromide (KBr) pallets of the respective samples.

NMR Spectroscopy: The $^{11}B\{^{1}H\}$ NMR spectra were obtained using a 600 MHz JEOL ECZ600R/M3 spectrometer. The compound was dissolved in a 2:1 mixture of DMF and deuterated methanol for NMR measurement, utilizing the automatic boron reference mode.

Raman spectroscopy: Raman spectra of M_9-COOH ligand were recorded using a CRM-Alpha 300S, WITec GmbH confocal Raman microscope, equipped with 532 nm frequency doubled Nd:YAG laser having an output power of 650 μW. This instrument was equipped with a Peltier cooled charge-coupled detector system.

X-ray Photoelectron Spectroscopy: XPS data were measured using an ESCA probe TPD equipped with a polychromatic Mg Kα X-ray source ($h\nu$ = 1253.6 eV). The binding energy of the spectral regions of different elements was calibrated with respect to C 1s (285.0 eV).

Femtosecond transient absorption studies: The femtosecond TA measurements were performed using an ultrafast short laser pulse (pulse width 120 fs) centered at 800 nm. The pulse was generated by spectra physics Maitai oscillator with a few hundred nJ energy. The output beam was sent to Ti: sapphire optical amplifier to produce high energy pulses (pulse energy 4 mJ, width 120 fs, repetition rate 1 kHz). The output beam is further split into two parts: the first high-energy beam produces the second harmonic using β-barium borate crystal. The obtained 400 nm pulses are used to excite the sample with an intensity of 250 μJ/cm^2. The second part of the beam was used to generate the white light continuum probe pulses (450-800 nm) by CaF_2 crystal. The computer-controlled motion controller creates the delay between pump and probe pulses. The absorbance changes in the probe beam are due to the pump being calculated using the equation-

$$\Delta A = \log\,[(s)/I_0(s)] — [I_{ex}(r)/I_0(r)]$$

Where, r and s correspond to the reference and sample, I_{ex} and I_o are transmitted intensities of probe pulse after excitation and in the ground state, respectively. The intensity of the transmitted pulse is measured with the help of MS 2004.

Single crystal X-ray Diffraction: Single-crystal diffraction data were collected on a Rigaku OD Supernova diffractometer using an Atlas S2 CCD detector and mirror collimated Mo-Kα (λ = 0.71073 Å) from a micro-focused sealed X-ray tube. The sample was cooled to 95 K during the measurement. Integration of the CCD images, absorption correction and scaling were performed by software CrysAlisPro. Crystal structures were solved by charge flipping with program SUPERFLIP and refined with the JANA2020 program package by full-matrix least-squares technique on F^2.[1,2] Hydrogen atoms were not visible in difference Fourier maps and were added from geometry. As per common practice hydrogen atoms attached to borons were kept in ideal positions during the refinement with B-H distance 1.00 Å. The isotropic atomic displacement parameters of hydrogen atoms were evaluated as 1.2Ueq of the parent atom.

All non-solvent and non-hydrogen atoms were refined harmonically. All hydrogen atoms were kept in the geometrically correct positions with the B–H distance of 1 Å. The isotropic atomic displacement parameters of hydrogen atoms were evaluated as 1.2*U_{eq} of the parent boron atom. Atoms Ag16 – Ag31 are disordered in two positions (labelled as “a” and “b”). For two atoms of silver (Ag31 and Ag29), a third position (labelled as “c”) was observed in the difference Fourier maps. Similarly, five surface sulfur atoms (S19 - S23) were also observed as disordered in two positions (labelled as “a” and “b”).

The disorder of carborane cages is modelled using rigid body approaches, where the 12-vertex carboranyl ($C_2B_{10}H_{11}$) cages were modeled as all boron $B_{12}H_{11}$ cages in 21 positions, some of which had partial occupancy. Distinguishing two carbon and 10 boron atoms in each cage was not possibly due to their negligible 1e difference and numerous disorders. All atoms in the vertices were nevertheless clearly visible in the difference Fourier map. There is a residual electron density near some Ag and B atoms, which could refer to even more complicated disorder. However, its modeling is not possible from current data.

Atoms of the solvent molecules (DMF) cannot be clearly distinguished in the electron density maps. Only oxygen atoms are depicted as they match the strongest maxima of the difference Fourier.

Table S1. Crystallographic parameters and refinement data for Ag_{62} nanocluster.

	Ag_{62} – at 95K
CCDC	**2374547**
Empirical formula	$Ag_{62}B_{320}C_{64}H_{352}S_{44}$
Diffractometer	four-cycle diffractometer Cryostream, AtlasS2, Rigaku OD Supernova
M_r /g mol^{-1}	12681.67 (formula weight)
T/K	95
Wavelength / Å	0.71073
Crystal system	Monoclinic
Space group	$P2_1/n$
a/Å	24.3524 (4)
b/Å	35.5608 (5)
c/Å	26.0322 (4)
α/deg	90
β/deg	91.0215 (14)
γ/deg	90
V/Å^3	22540.1 (6)
Z	2

	Ag₆₂ – at 95K
Calc. density/g cm^{-3}	1.904
μ mm^{-1}	2.86
F(000)	12100
Crystal size /mm^3	0.19 × 0.09 × 0.08
θ range /°	2.3–26.6°
Index ranges /*hkl*	-33-33, -46-48, -28-32
Reflections collected (R_{int})	0.109
Independent reflections	55437
Completeness /% to θ /°	98, 27.61
Absorption correction	Multi-scan
Max. and min. transmission	Tmin = 1.9, Tmax = 29.7
Data / restraints / constraints / parameters	55437/1/395/632
Goodness-of-fit on F^2	2.28
*R*1, *wR*2 [I>3σ(I)]	0.1474, 0.2800
*R*1, *wR*2 (all data)	0.3006, 0.3202
Largest diff. peak and hole, eÅ^{-3}	5.83, −4.15

Theoretical calculation

Theoretical calculations were done using density functional theory (DFT) as implemented in software GPAW.[3,4] We used real space grid with 0.2 Å grid spacing and Perdew-Ernzerhof-Burke (PBE) exchange correlation functional in structure optimization that was done for the crystal structure.[5] Structure was optimized until the forces acting on atoms were below 0.05 eV/Å. After structure optimization the further analysis was done using GLLB-sc xc-functional.[6] Density of states was projected to spherical harmonics functions centered at the center of the mass of the cluster.[7] Optical absorption spectra were calculated using linear response time dependent density functional theory (LR-TDDFT) using PBE xc-functional as a LR-TDDFT kernel.[3,8] Origin of the peaks of the absorption spectra were analysed using dipole transition contribution maps which is showing the strengthening and screening contributions to total transition dipole moment as decomposed to Kohn-Sham basis.[9]

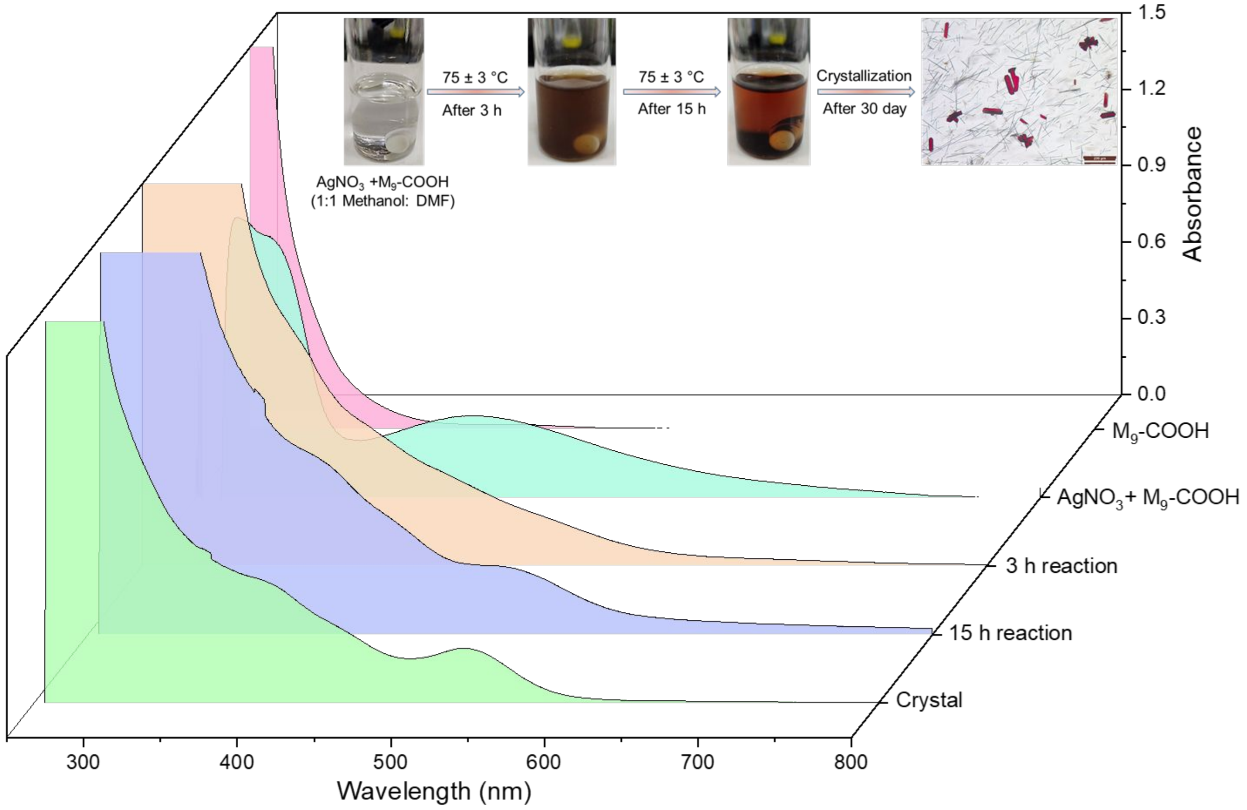

Figure S1. The comparative UV-vis absorption spectra of the M_9-COOH ligand and intermediate species formed during the synthesis of Ag_{62} nanocluster. Inset shows the photographs capturing the reaction vial at different stages throughout the synthesis process. An optical micrograph displays rod-shaped Ag_{62} crystals.

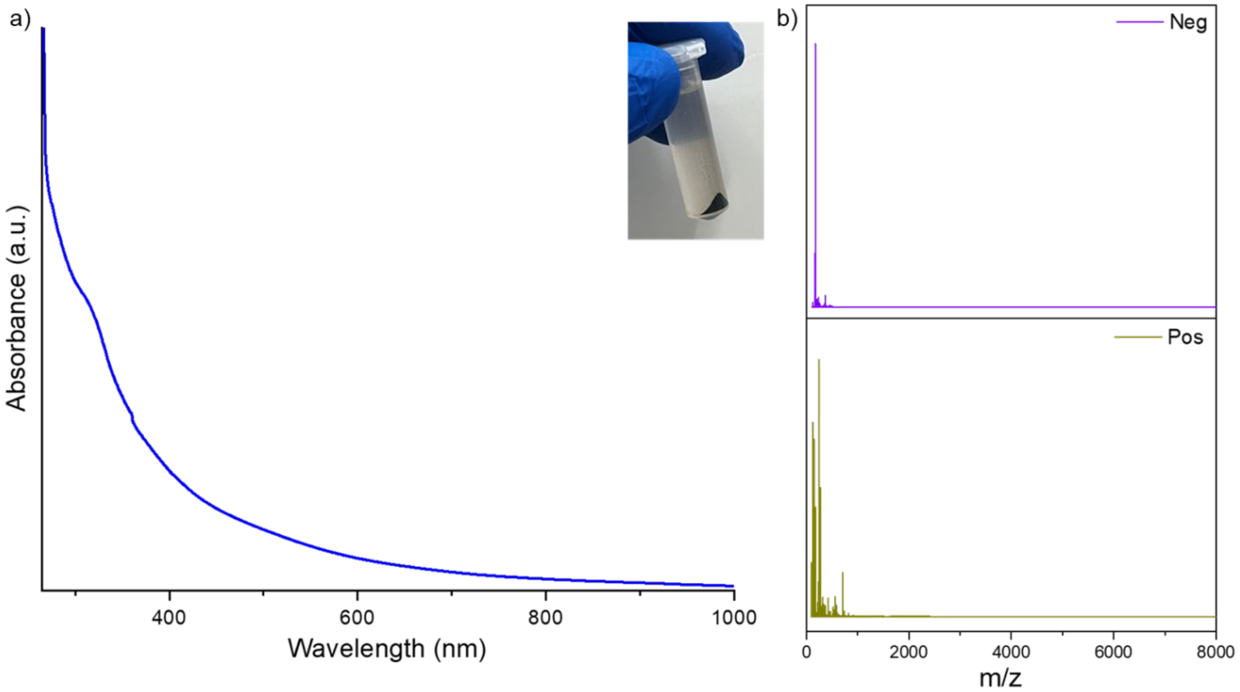

Figure S2. a) The UV-vis absorption spectrum of the synthesized product obtained from the solvothermal reaction of $AgNO_3$ and M_9 ligand. Inset shows the photograph of the crude product. b) The comparative ESI-MS spectra of the same reaction product revealed an absence of distinct features.

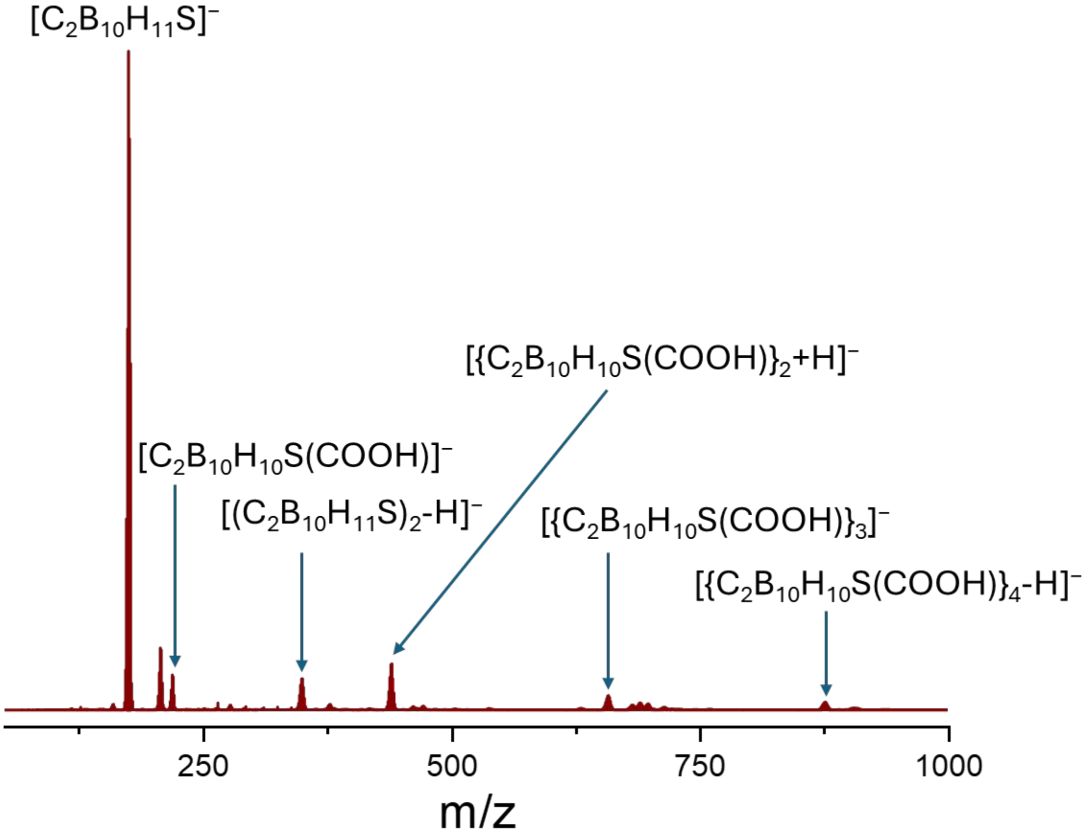

Figure S3. The negative ion mode ESI-mass spectrum of the M_9-COOH ligand was obtained by dissolving it in a solution of dichloromethane and methanol (1:1 v/v). The spectrum revealed a molecular ion peak at m/z 219.17, along with peaks indicating di (m/z 439.31), tri (m/z 658.41), and tetrameric (m/z 875.61) polymerization of the M_9-COOH. This polymerization is primarily attributed to hydrogen bonding of the -COOH groups and disulfide linkages.

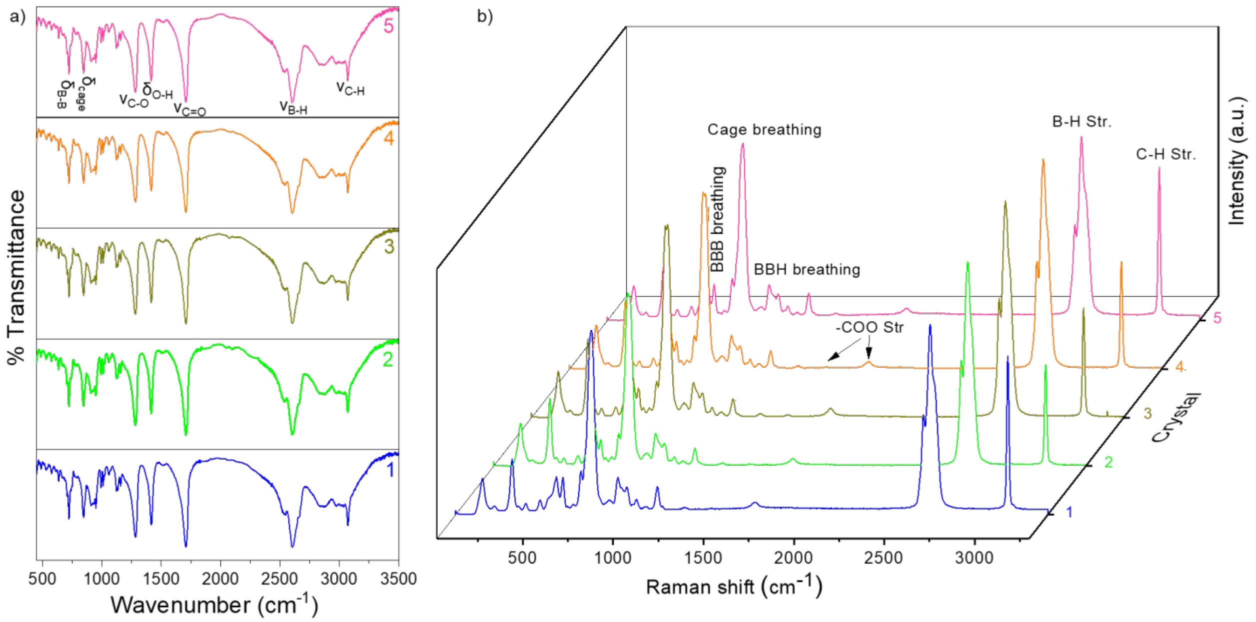

Figure S4. Comparative a) IR and b) Raman spectra of five different samples of M_9-COOH ligands show the presence of an acid group associated with the carborane cage in the ligand.

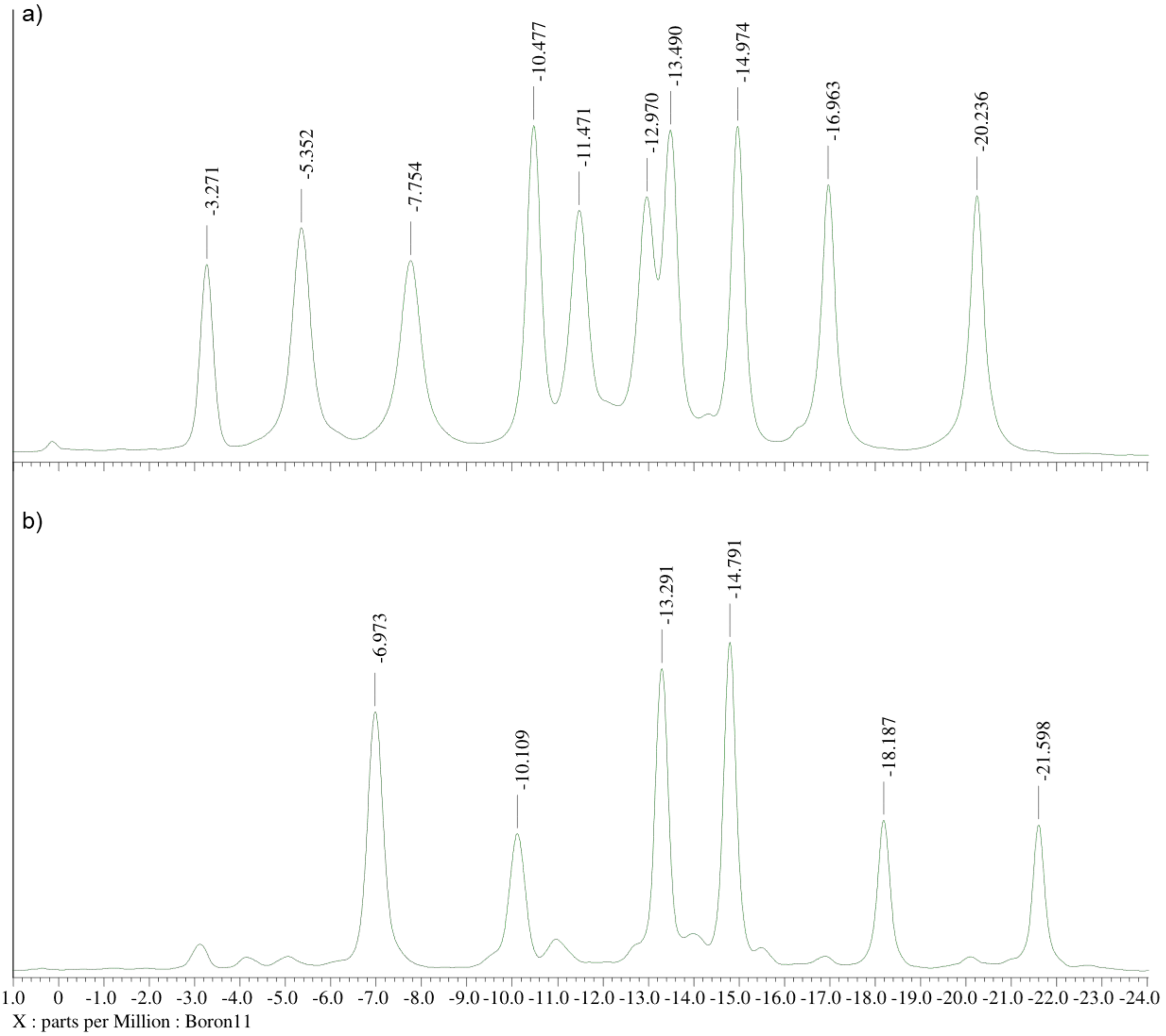

Figure S5. The comparative $^{11}B\{^{1}H\}$ NMR spectra of the M_9-COOH ligand (dissolved in 2:1 DMF: deuterated methanol) are presented as follows: a) before thermal treatment and b) after thermal treatment at 55 °C.

The ^{11}B NMR peaks of M_9-COOH before treatment appear at the following chemical shift values: -3.271, -5.352, -7.754, -10.477, -11.471, -12.970, -13.490, -14.974, -16.963, and -20.236 ppm, all in a 1:1:1:1:1:1:1:1:1:1 ratio. After thermal treatment, these peaks shift to -3.08, -6.973, -10.109, -13.291, -14.791, -18.187, and -21.598 (in 1:2:1:2:2:1:1 ratio), indicating a clear decarboxylation of the ligand as a result of the thermal treatment.

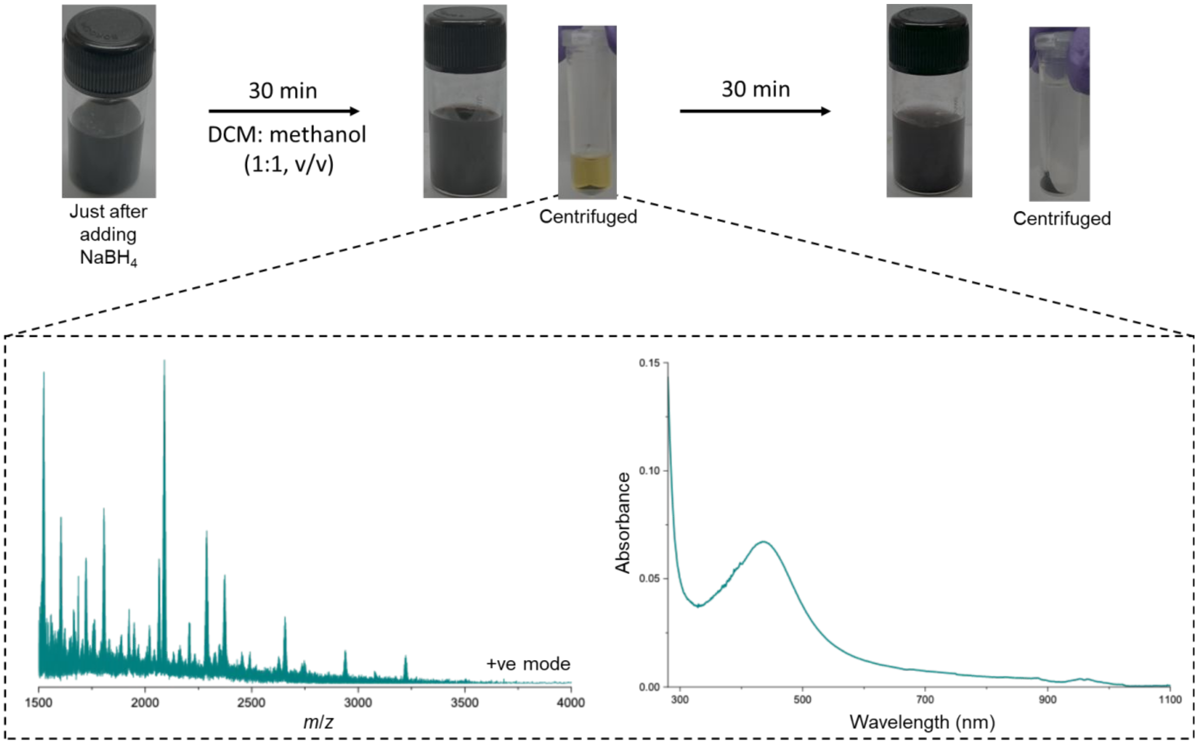

Figure S6. Photographs capturing the different stages of the direct reduction process of $AgNO_3$ and M_9 precursors, utilizing $NaBH_4$ as reducing agent. The inset features the positive ion mode ESI mass spectrum and UV-vis absorption spectrum of a slightly orange solution that formed after 30 minutes of reaction.

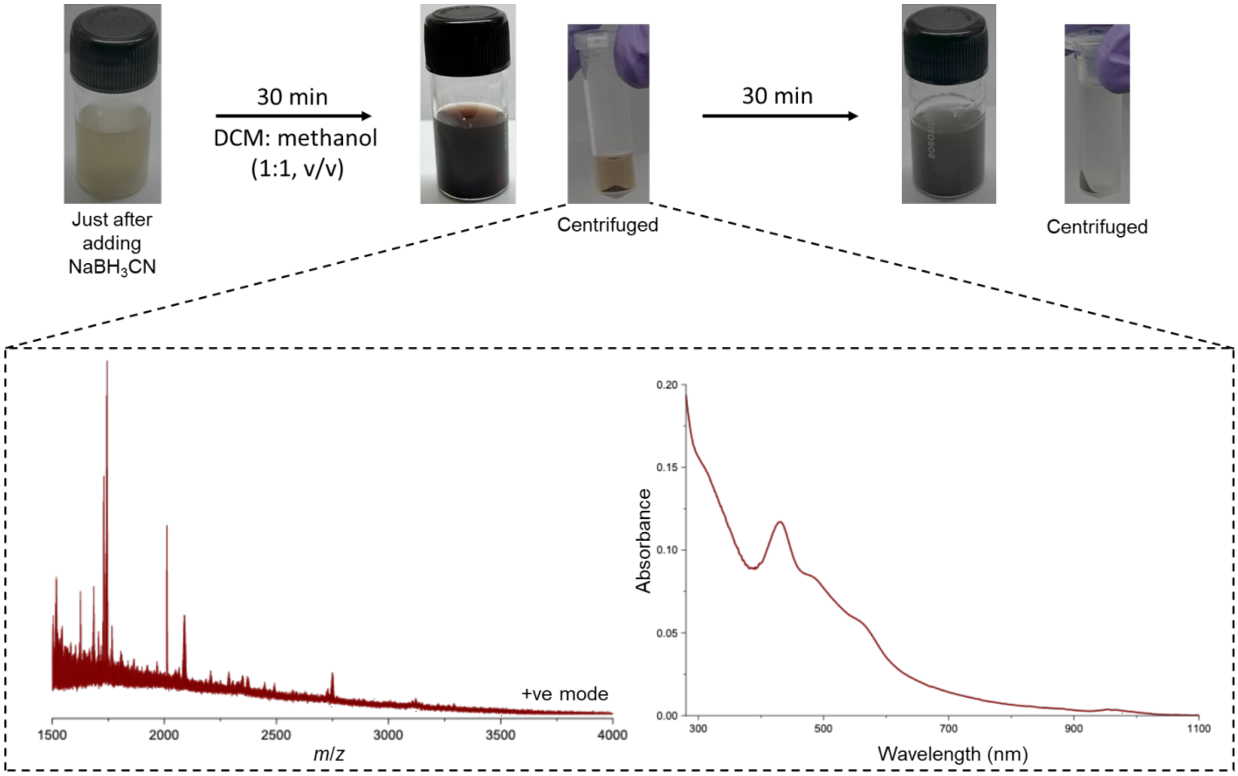

Figure S7. Photographs capturing the different stages of the direct reduction process of $AgNO_3$ and M_9 precursors, utilizing $NaBH_3CN$ as reducing agent. The inset features the positive ion mode ESI mass spectrum and the UV-vis absorption spectrum of a slightly orange solution that formed after 30 minutes of reaction.

a)

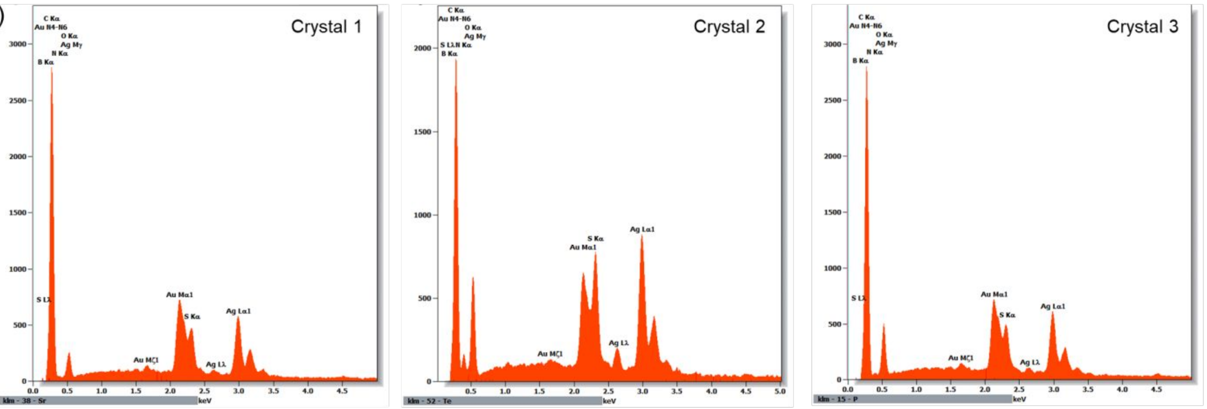

b)

Element			
	Net Counts	Weight %	Atom %
B K	330	5.92	7.05
C K	16365	26.04	45.17
N K	352	6.74	7.33
O K	3981	15.29	19.13
S K	8903	6.12	6.62
Ag L	8161	22.88	8.37
Au L	1245	17.01	6.33
		100.00	100.00

Element			
	Net Counts	Weight %	Atom %
B K	389	6.15	7.62
C K	17992	28.81	47.16
N K	339	2.99	4.85
O K	2973	9.29	19.11
S K	5097	3.98	6.33
Ag L	8505	21.86	8.72
Au L	1721	26.92	6.21
		100.00	100.00

Element			
	Net Counts	Weight %	Atom %
B K	360	5.68	6.81
C K	17164	25.17	48.50
N K	345	4.50	5.48
O K	2488	8.90	17.15
S K	4807	7.28	6.49
Ag L	8386	23.52	8.60
Au L	1592	24.95	6.97
		100.00	100.00

Figure S8. a) The EDS spectra measured from three different single crystals of Ag_{62} nanocluster. b) The content of the elements present in the crystals are shown here. The Au content is due the effect of gold sputtering onto the crystal.

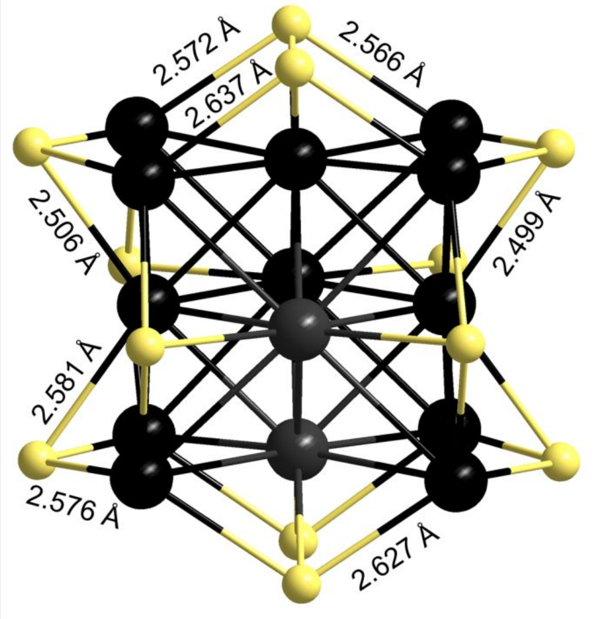

Figure S9. The Ag_{14}-S_{12} inner skeleton of the Ag_{62} nanocluster with marked Ag–S distances. Color code as, black: Ag, yellow = S.

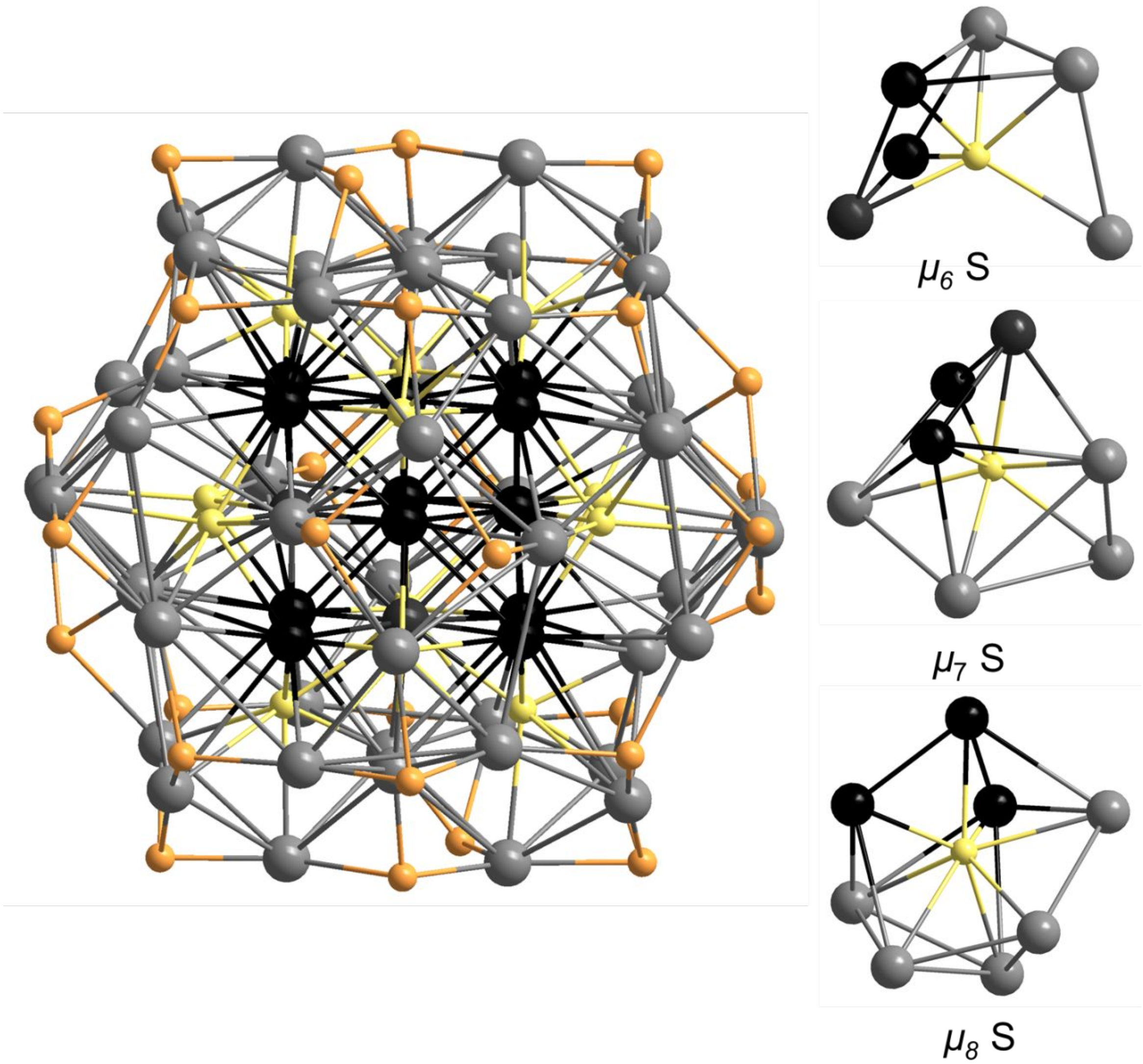

Figure S10. Various types of silver-sulfide bonding of twelve inner sulfide atoms present in the Ag_{62} nanocluster.

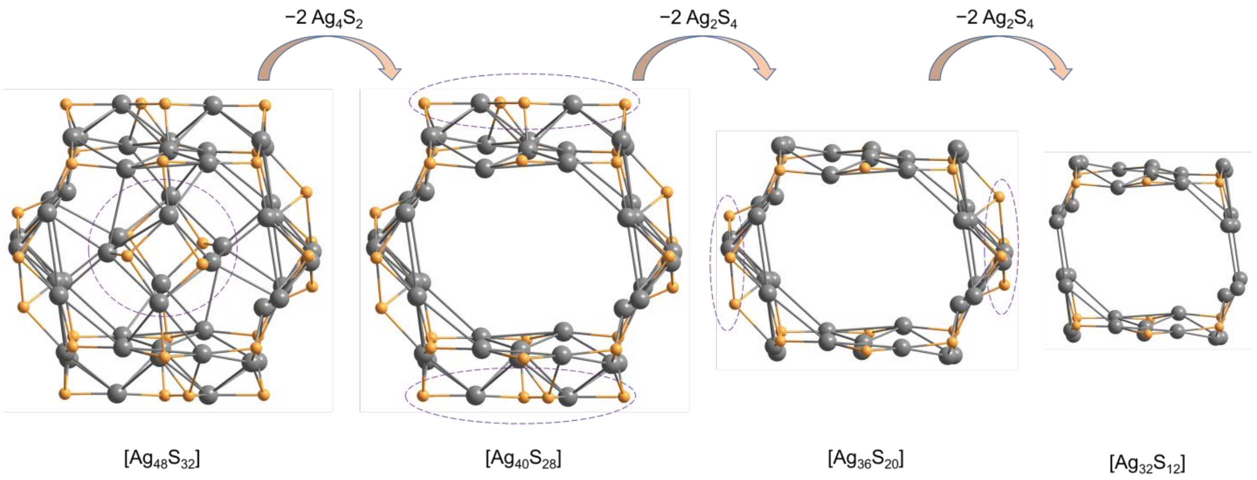

Figure S11. Sequential fragmentation of outer [$Ag_{48}S_{32}$] skeleton of the Ag_{62} nanocluster.

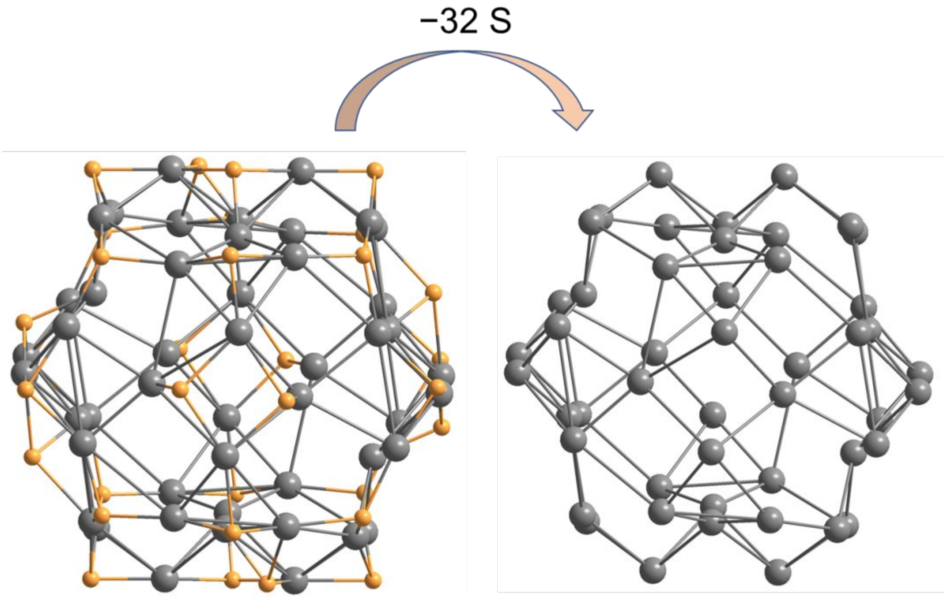

Figure S12. The outer [$Ag_{48}S_{32}$] skeleton of the Ag_{62} nanocluster with and without thiolated S atoms.

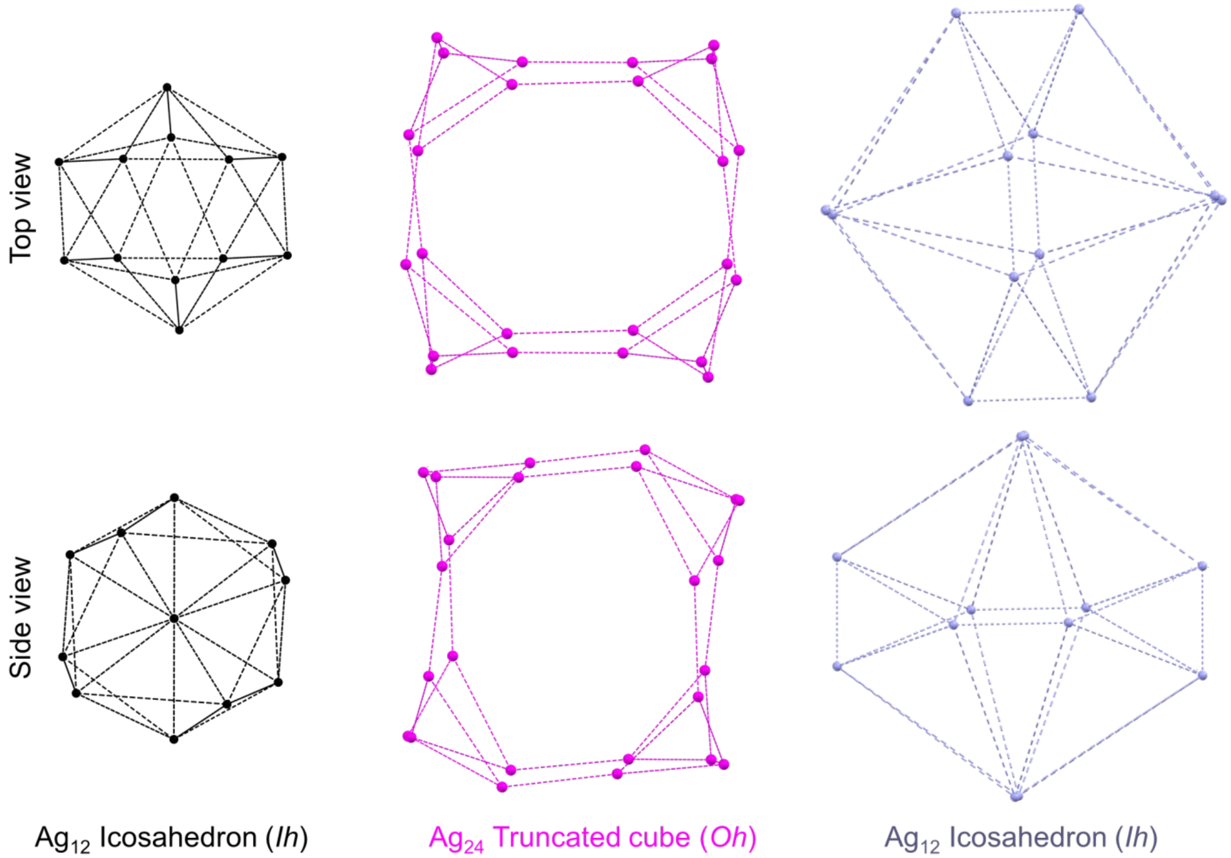

Ag_{12} Icosahedron (*Ih*) Ag_{24} Truncated cube (*Oh*) Ag_{12} Icosahedron (*Ih*)

Figure S13. An independent view of three different symmetry elements in the outer Ag_{48} skeleton. All of these atoms are Ag.

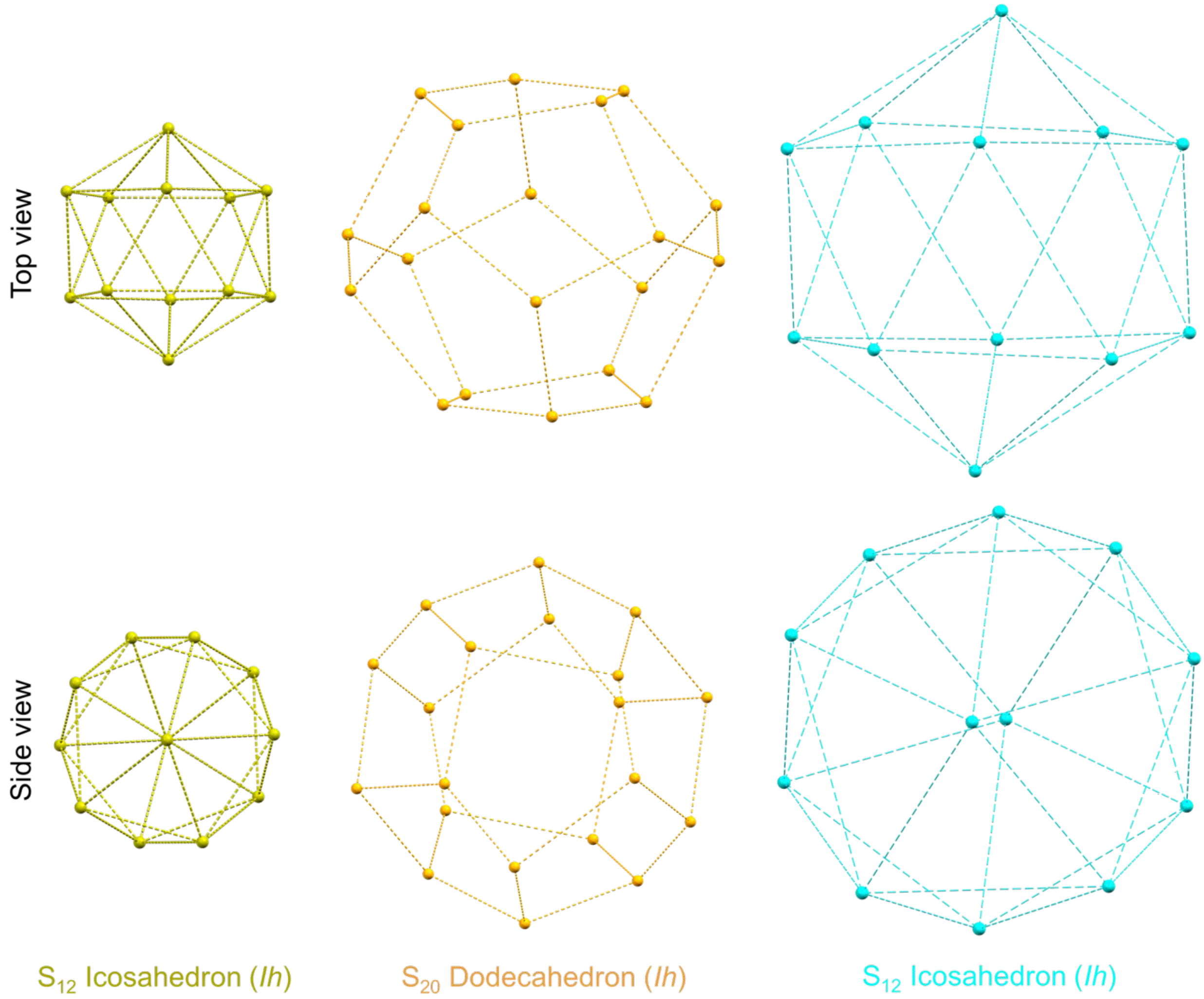

Figure S14. An independent view of three symmetry elements in the inner S_{12} and outer S_{32} (S_{20} and S_{12}) skeletons. All of these atoms are S.

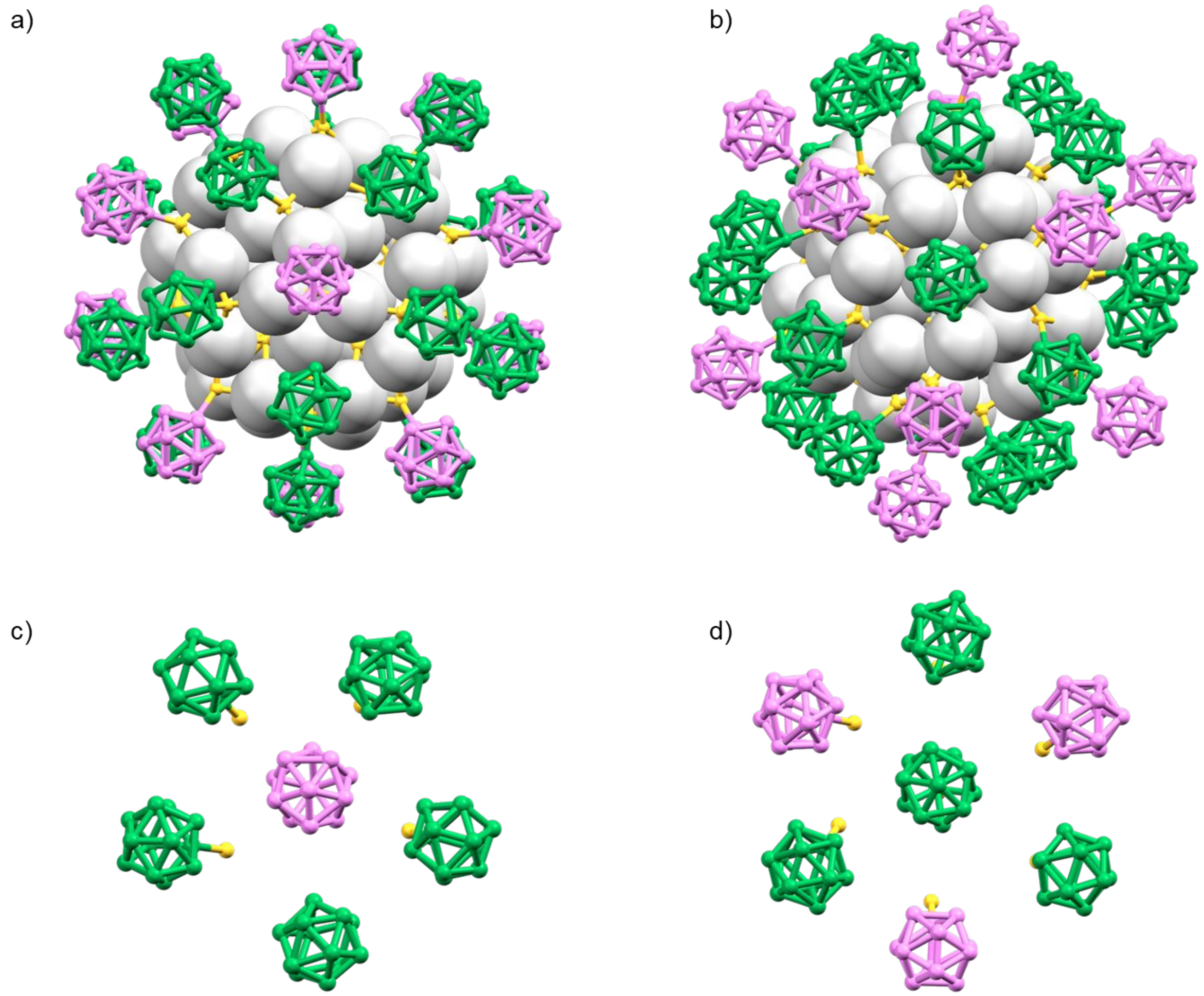

Figure S15. a) Distribution of carboranes (pink in color) encircled by five additional nearby carboranes. b) Distribution of carboranes (green in color) encircled by six additional nearby carboranes. Hydrogen atoms are removed for clarity. c and d) Corresponding pentagonal and hexagonal assembly of carboranes. Silver atoms are omitted for clarity.

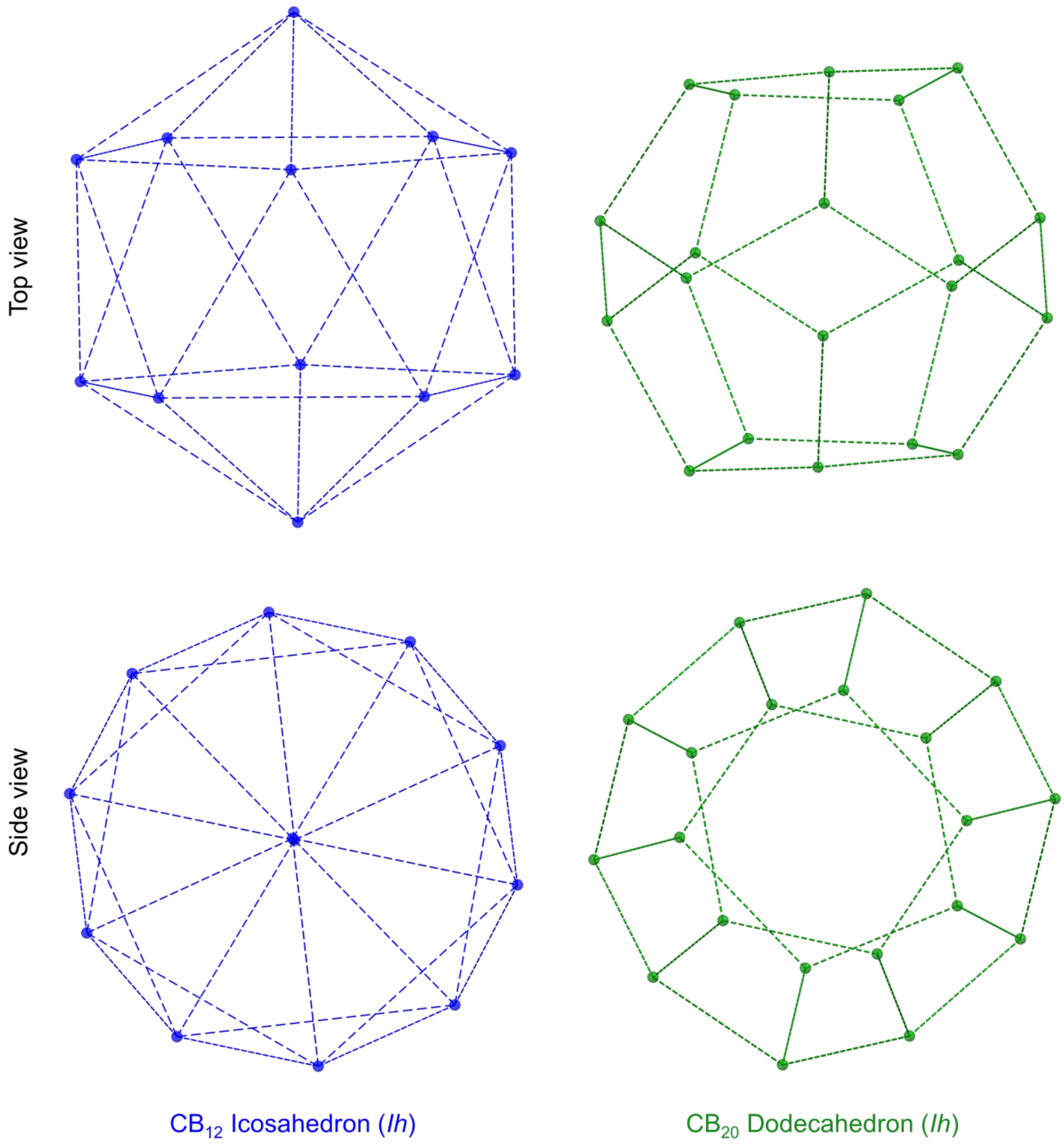

Figure S16. An independent view of the two types of symmetry present in the centroids of 32 carboranes. All of these points are the centroids of each carborane.

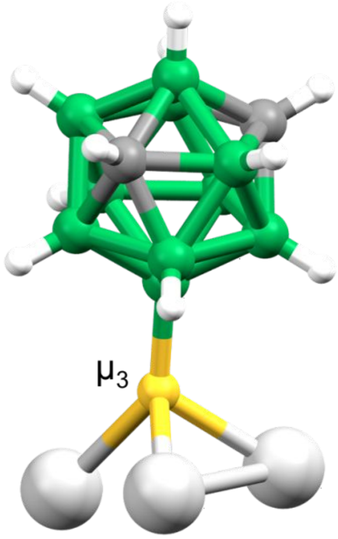

Figure S17. Silver-sulfide bonding of the outer thiolated S atoms connected with carborane ligands.

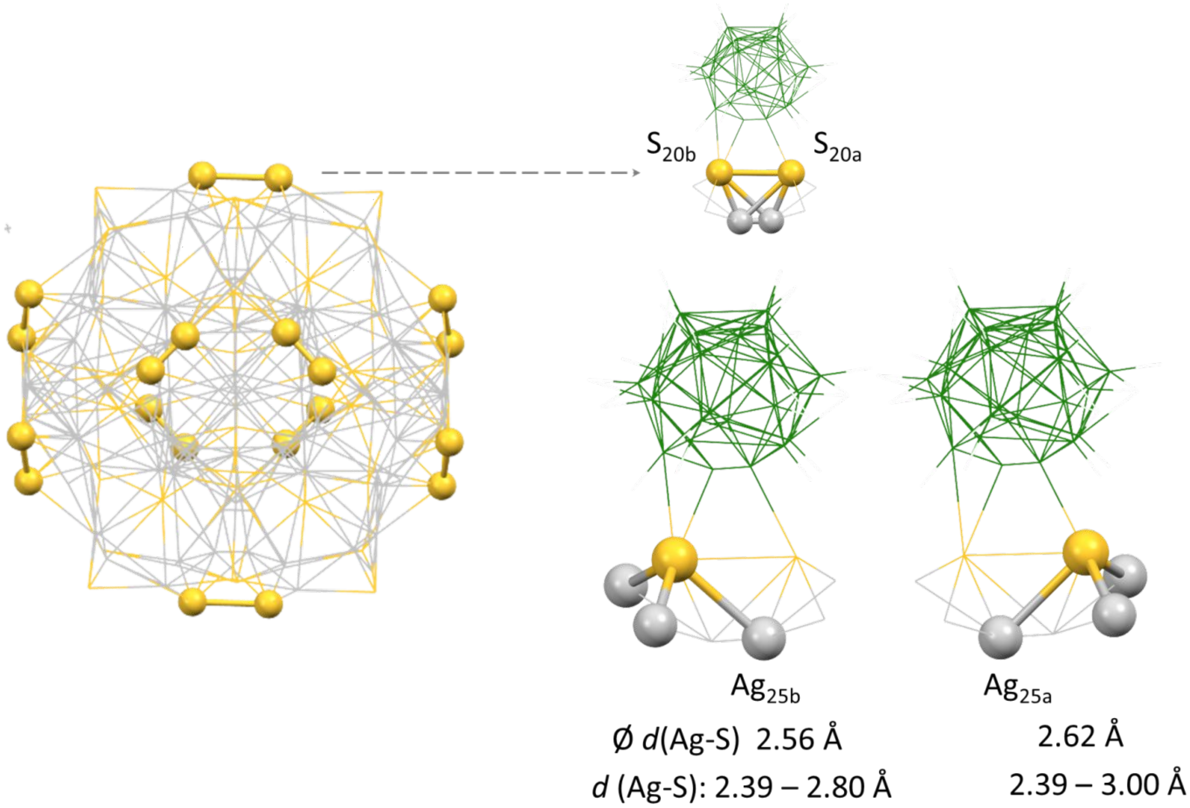

Figure S18. Disorder of S atoms in the outer silver sulfide skeleton of the Ag_{62} nanocluster.

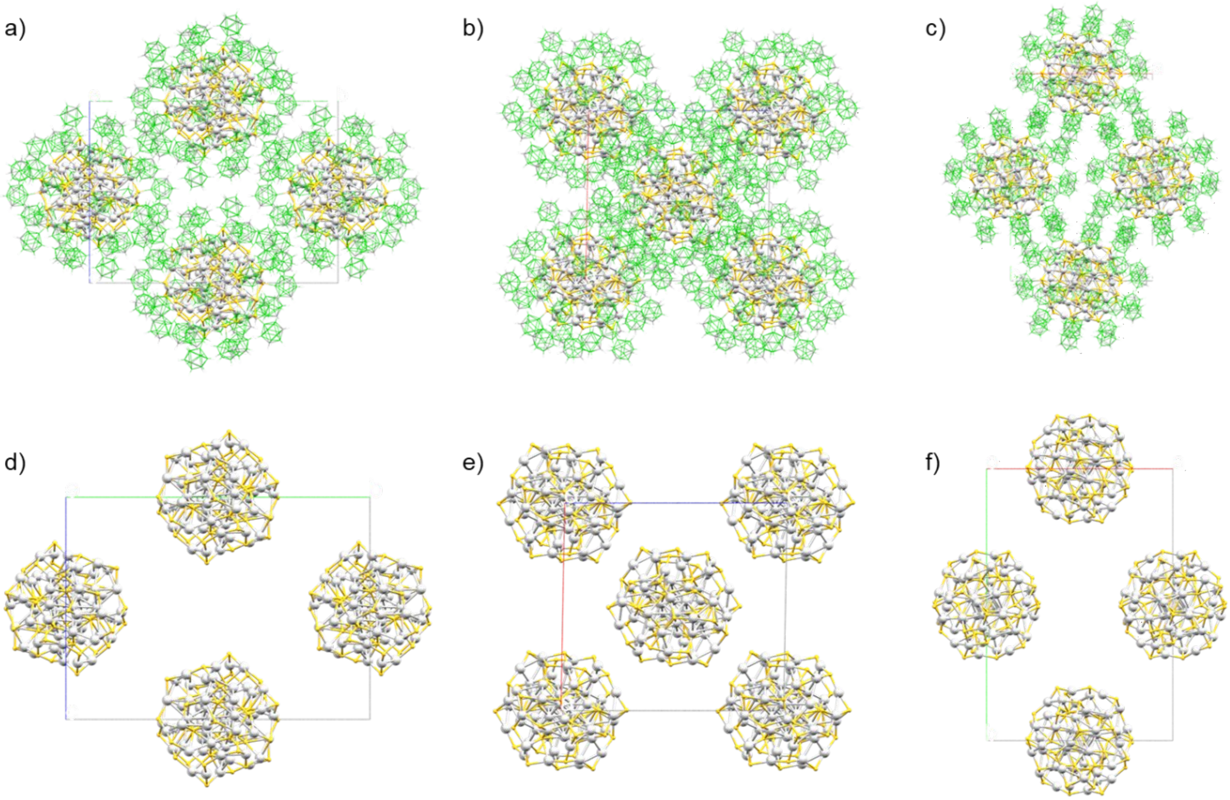

Figure S19. Unit cell molecular packing of the Ag_{62} nanocluster along a) a, b) b, and c) c crystallographic axis. Unit cell packing of the silver-sulfide skeleton along d) a, e) b, and f) c crystallographic axis.

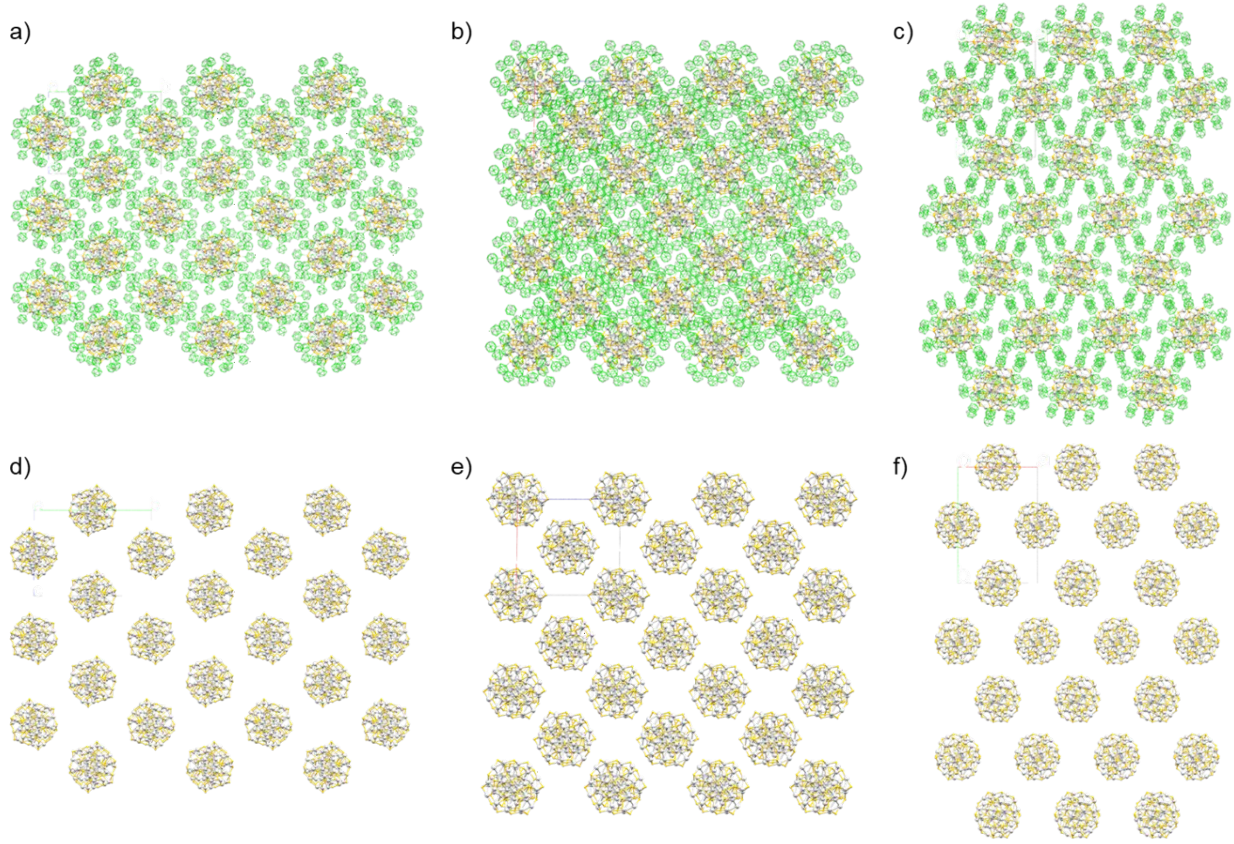

Figure S20. Extended (3×3×3) supramolecular packing of the Ag_{62} nanocluster along a) a, b) b, and c) c crystallographic axis. The packing of the silver sulfide skeleton along d) a, e) b, and f) c crystallographic axis.

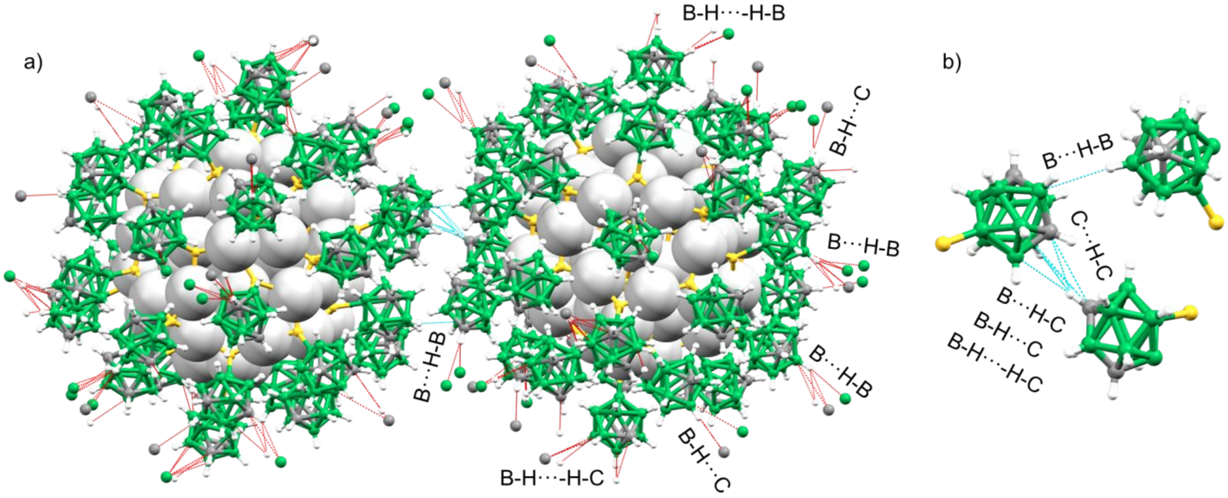

Figure S21. a) Various types of intermolecular interactions present in the crystal lattice. b) Expanded view of carborane centered interactions responsible for supramolecular packing of the clusters.

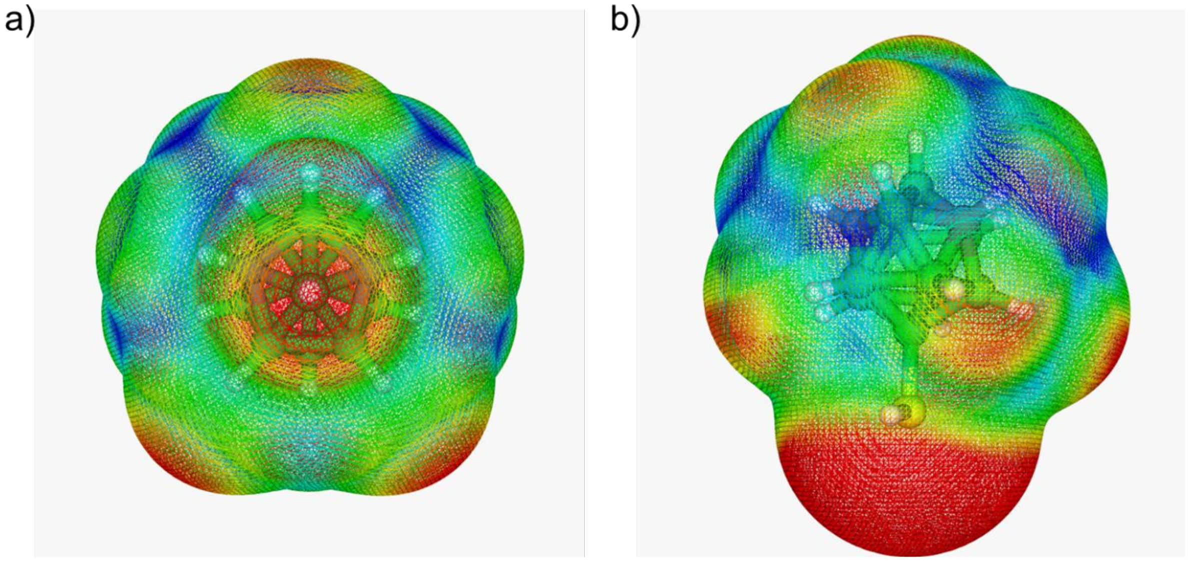

Figure S22. Molecular electrostatic potential mapped on an isosurface of the electron density for *meta*-carborane-9-thiol ligand. a: top view, b: side view.

The molecular electrostatic potential mapped on an isosurface of the electron density offers valuable insight into the nature of intermolecular interactions and, by extension, the arrangement between the carborane shells of the $[Ag_{62}S_{12}(CBT)_{32}]^{4+}$ clusters. This figure shows a single molecule of the CBT-H ligand from two perspectives. The top view illustrates how the molecule is oriented toward the outer environment while the side view highlights interactions between neighboring carborane molecules within the ligand shell of metal cluster. Regions in red represent areas of lowest electrostatic potential. In addition to sulfur atoms (which are buried beneath the carborane units on the metal cluster surface), B–H vertices also appear red which corresponds with their hydridic character ($B–H^{\delta-}$), whereas hydrogen atoms bonded to carbon atoms are positively charged ($C–H^{\delta+}$).

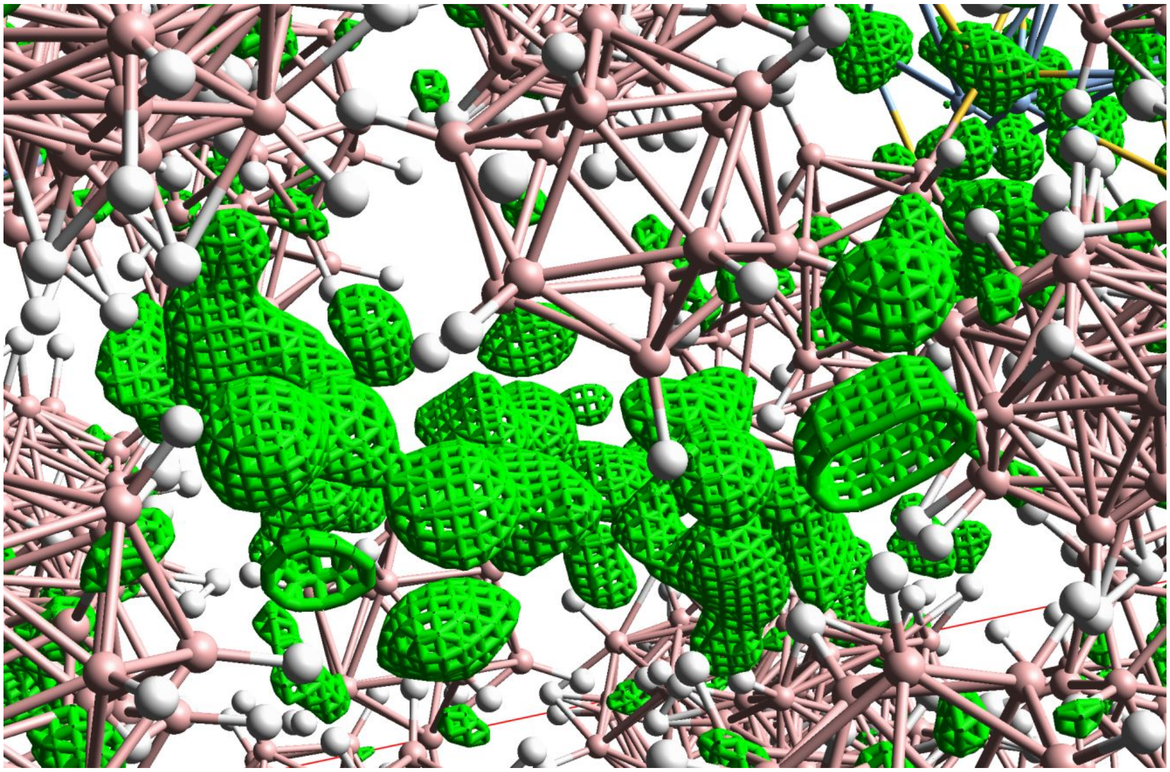

Figure S23. Residual electron density maps of the solvent molecules or counter ions present in the crystal lattice of Ag_{62} nanocluster.

Table S2. A summary of the structurally resolved carborane thiol- and alkynyl-protected metal (gold, silver, copper and alloy) nanoclusters.

Sl. No	Composition	Ligand used	Crystal system (space group)	Core @ shell structure	Ref
1.	$[Ag_{14}(C_2B_{10}H_{10}S_2)_6(CH_3CN)_8]$	*ortho*-carborane 1, 2-dithiol	Triclinic (P-1)	Ag_6 octahedron @ Ag_8 cube	10
2.	$[Ag_{14}(C_2B_{10}H_{10}S_2)_6(\text{pyridine})_8]$	*ortho*-carborane 1, 2-dithiol	Tetragonal ($I4/m$)	Ag_6 octahedron @ Ag_8 cube	10
3.	$[Ag_{14}(C_2B_{10}H_{10}S_2)_6(\text{methyl-pyridine})_8]$	*ortho*-carborane 1, 2-dithiol	Orthorhombic ($Pbca$)	Ag_6 octahedron @ Ag_8 cube	10
4.	$[Ag_{14}(C_2B_{10}H_{10}S_2)_6(PPh_3)_6]$	*ortho*-carborane 1, 2-dithiol	Triclinic (P-1)	Ag_8 @ Ag_6 isolated	11
5.	$[Ag_{14}(C_4B_{10}H_{11})_{12}(CH_3CN)_2]$	9-alkynyl *ortho*-carborane	Monoclinic ($C2/c$)	Ag_8 cube @ Ag_6 octahedron	12
6.	$[Cu_6Ag_8(C_4B_{10}H_{11})_{12}(CH_3CN)_2]$	9-alkynyl *ortho*-carborane	Cubic ($Im\bar{3}$)	Ag_8 cube @ Cu_6 octahedron	12
7.	$[Cu_{14}(C_2B_{10}H_{10}S_2)_6(CH_3CN)_8]$	*ortho*-carborane 1, 2-dithiol	Cubic ($Fm\bar{3}m$)	Cu_6 octahedron @ Cu_8 cube	13
8.	$[Cu_{14}(S_2C_2B_{10}H_{10})_6(DMF)_6O_2]$	*ortho*-carborane 9, 12-dithiol	Trigonal (R-3:H)	Cu_6 octahedron @ Cu_8 cube	14
9.	$[Cu_{16}(C_2B_{10}H_{10}S_2)_8]$	*ortho*-carborane 9, 12-dithiol	Monoclinic ($P2_1/n$)	Cu_{12} drum with 4 capping Cu	15
10.	$[Cu_{14}(C_2B_{10}H_{10}S_2)_6(CH_3CN)_6]$ and $[Cu_{16}(C_2B_{10}H_{10}S_2)_8]$ cocrystal	*ortho*-carborane 9, 12-dithiol	Tetragonal ($P42_12$)	-	16
11.	$[Ag_{17}I_3S(C_2B_{10}H_{10}S_2)_6(CH_3CN)_{11}]$	*ortho*-carborane 1, 2-dithiol	Hexagonal ($P6_3/m$)	Ag_6S central triangular prism @ Ag_{11} isolated	17
12.	$[Cu_{17}I_3S(C_2B_{10}H_{10}S_2)_6(CH_3CN)_{11}]$	*ortho*-carborane 1, 2-dithiol	Hexagonal ($P6_3$/m)	Cu_6S central triangular prism @ Cu_{11} isolated	17
13.	$[Ag_{21}(C_2B_{10}H_{11}S)_{12}(PPh_3)_2]$	*meta*-carborane 9-thiol	Cubic ($Pa\bar{3}$)	Ag_{13} central icosahedral @ Ag_6-Ag_2 motifs	18
14.	$[Au_{23}(C_4B_{10}H_{11})_9(\text{tht})_6]$	9-alkynyl *ortho*-carborane	Monoclinic ($P2_1/n$)	Au_{17} kernel and three $[Au_2(C_4B_{10}H_{11})_3]$ motifs	19
15.	$[Au_{28}(C_4B_{10}H_{11})_{12}(\text{tht})_8]$	9-alkynyl *ortho*-carborane	Triclinic (P-1)	Au_4 tetrahedron and truncated Au_{24} tetrahedron	19

16.	$[Au_{28}(C_2B_{10}H_{11}S)_{12}(tht)_4Cl_4]$	*ortho*-carborane 1-thiol	Tetragonal ($\mathrm{P}2_1c$)	Au_{12} kernel and two saddle-shaped Au_8 motifs	20
17.	$[Ag_{30}(C_2B_{10}H_9S_3)_8DPPM_6]$	*ortho*-carborane 8, 9, 12 trithiol	Trigonal ($P31c$)	Triangular Ag_3 surrounded by crown like Ag_{27} motifs	21
18.	$[Ag_{33}(C_2B_{10}H_{10}S_2)_{12}]$	*ortho*-carborane 9, 12-dithiol	Trigonal (R-3)	Ag_{13} central icosahedral @ Ag_{20} dodecahedron	22
19.	$[Ag_{13}Ag_{14}Cu_6(C_2B_{10}H_{10}S_2)_{12}(CH_3CN)_2]$	*ortho*-carborane 9, 12-dithiol	Orthorhombic ($P2_12_12_1$)	Ag_{13} central icosahedral @ $Ag_{14}Cu_6$ distorted dodecahedron	22
20.	$[Ag_{13}Cu_{20}((C_2B_{10}H_{10}S_2)_{12}]$	*ortho*-carborane 9, 12-dithiol	Cubic ($Im\bar{3}$)	Ag_{13} central icosahedral @ Cu_{20} dodecahedron	22
21.	$[Cu_4(SC_2B_{10}H_{11})_4]$	*ortho*-carborane 9-thiol	Trigonal ($P3_121$)	Cu_4 square planner	23
22.	$[Cu_4(SC_2B_{10}H_{11})_4]$	*meta*-carborane 9-thiol	Monoclinic ($P2_1/c$)	Cu_4 square planner	23
23.	$[Cu_4I_3(SC_2B_{10}H_{11})_4]$	*ortho*-carborane 12-iodo 9-thiol	Tetragonal ($P4_32_12$)	Cu_4 square planner	23
24.	$[Cu_{20}(C_4B_{10}H_{11})_{16}(OC_3H_6)_2]$	9-alkynyl *ortho*-carborane	Monoclinic ($P2_1/c$)	Two fused Pentagonal bipyramids @ two Cu_3 triangles	24
25.	$[Cu_{14}(C_4B_{10}H_{11})_{10}(OC_3H_6)_6]$	9-alkynyl *ortho*-carborane	Triclinic (P-1)	Two shared pentagonal bipyramids @ two capping Cu atoms	24
26.	$[Cu_{13}(C_4B_{10}H_{11})_{10}(PPh_3)_2(CH_3CN)_2]$	9-alkynyl *ortho*-carborane	Triclinic (P-1)	Pentagonl pyramid shared with a pentagonal bipyramid @ two capping Cu atoms	24
27.	$[Cu_{26}(C_4B_{10}H_{11})_{16}(C_2B_9H_{10}C_2)_2(PPh_3)_2(CH_3CN)_4]$	9-alkynyl *ortho*-carborane	Triclinic (P-1)	Dimer of Cu_{13}	24
28.	$[Ag_{17}(SC_2B_{10}H_{11})_{12}]$	*ortho*-carborane-1-thiol	Orthorhombic ($Pbcn$)	Central icosahedral Ag_{13}@ four	25

				capping Ag atoms	
29.	$[AuAg_{16}(SC_2B_{10}H_{11})_{12}]$	*ortho*-carborane-1-thiol	Trigonal (*R*-3)	Central icosahedral $AuAg_{12}$@ four capping Ag atoms	25
30.	$[Ag_{13}Cu_4(SC_2B_{10}H_{11})_{12}]$	*ortho*-carborane-1-thiol	Triclinic (*P*-1)	Central icosahedral Ag_{13}@ four capping Cu atoms	25
31.	$[AuAg_{12}Cu_4(SC_2B_{10}H_{11})_{12}]$	*ortho*-carborane-1-thiol	Cubic ($Fd\bar{3}$)	Central icosahedral $AuAg_{12}$@ four capping Cu atoms	25
28.	**$[Ag_{62}S_{12}(SC_2B_{10}H_{11})_{32}]$**	***meta-carborane-9-thiol 12-carboxilic acid***	**Monoclinic ($P2_1/n$)**	**$Ag_{14}S_{12}$ core @ $Ag_{48}(CBT)_{32}$ shell**	**This work**

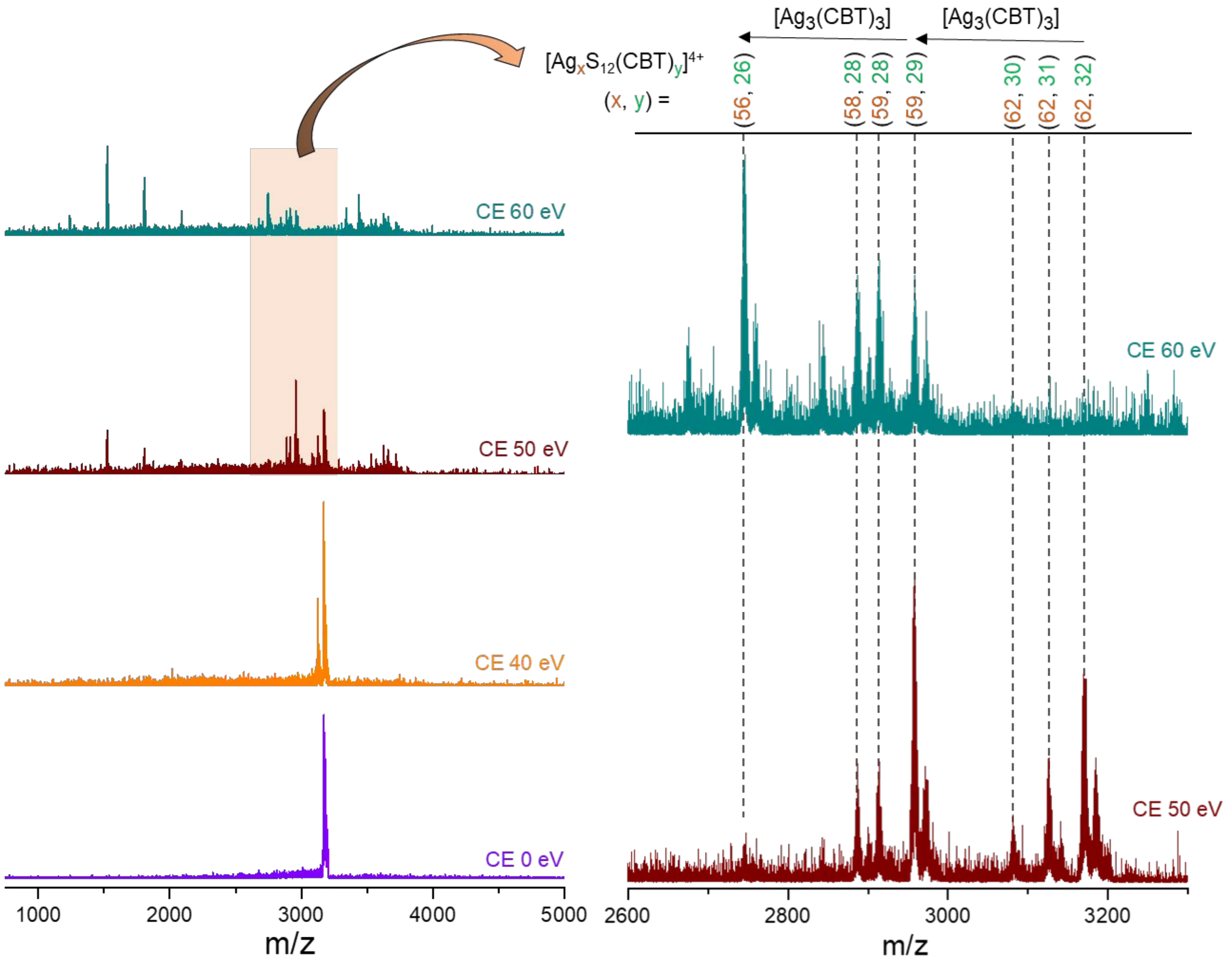

Figure S24. Collision energy dependent MS-MS fragmentation pattern upon selectin the primary peak at m/z 3170.42 having a charge state of 4+. Inset shows the expanded view of the highlighted region of the fragmentation spectra. Assignment of the molecular composition of the respective fragments are shown here. The weak ion intensity and broad isotopic distribution of the fragmented peaks [(62, 31), (62, 30), (59, 28) and (58, 28)] allowing for the possibility of additional proton attachment with them for balancing the 4+ charge state.

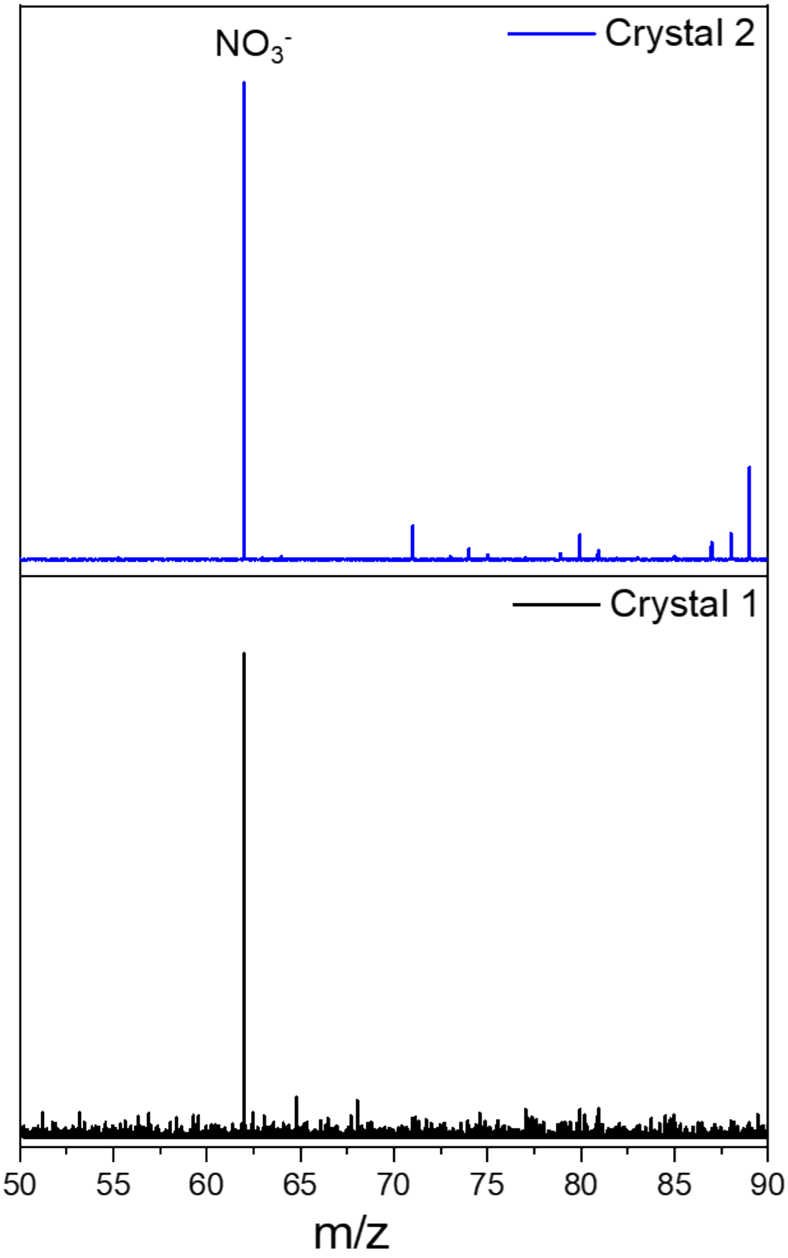

Figure S25. The negative ion mode ESI-MS spectra of two distinct set of Ag_{62} crystals reveal the presence of nitrate as counter ions.

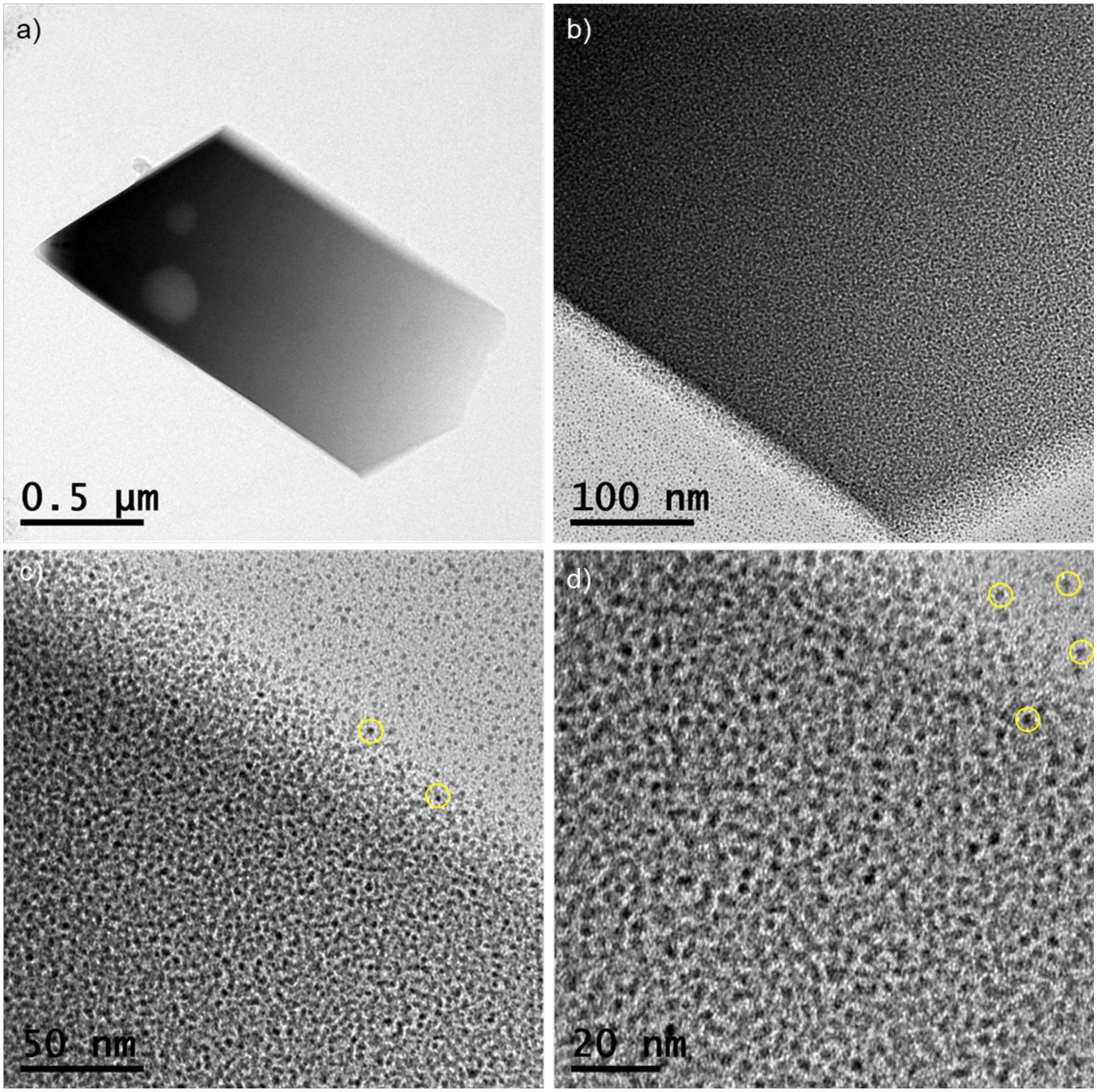

Figure S26. a) High resolution TEM micrograph of a cuboidal Ag_{62} crystal. b-d) Progressive magnification of an ultrathin edge of the crystal reveals the presence of uniform particles with an average diameter of 1.4±0.1 nm.

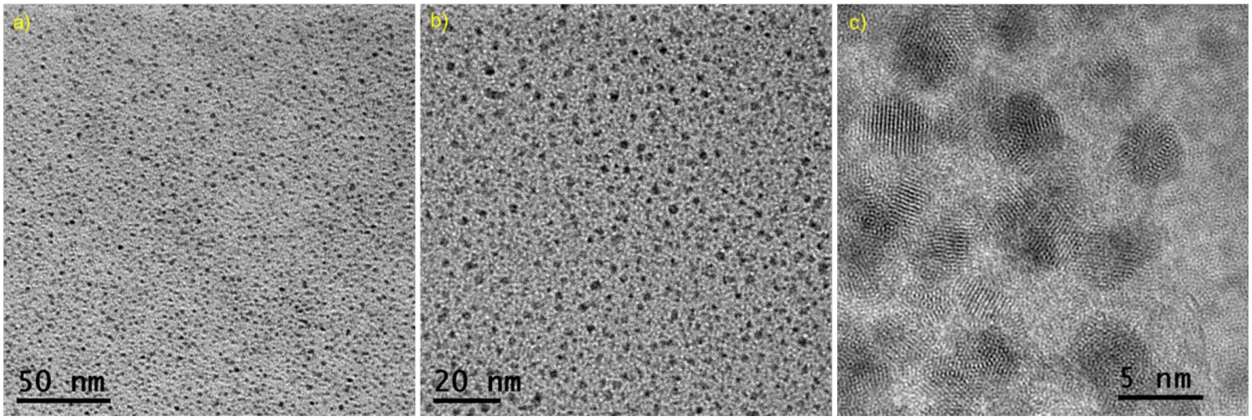

Figure S27. TEM images obtained from the drop-cast solution of Ag_{62} clusters at various magnifications show beam-induced aggregation and a corresponding size increase of the nanocluster particles.

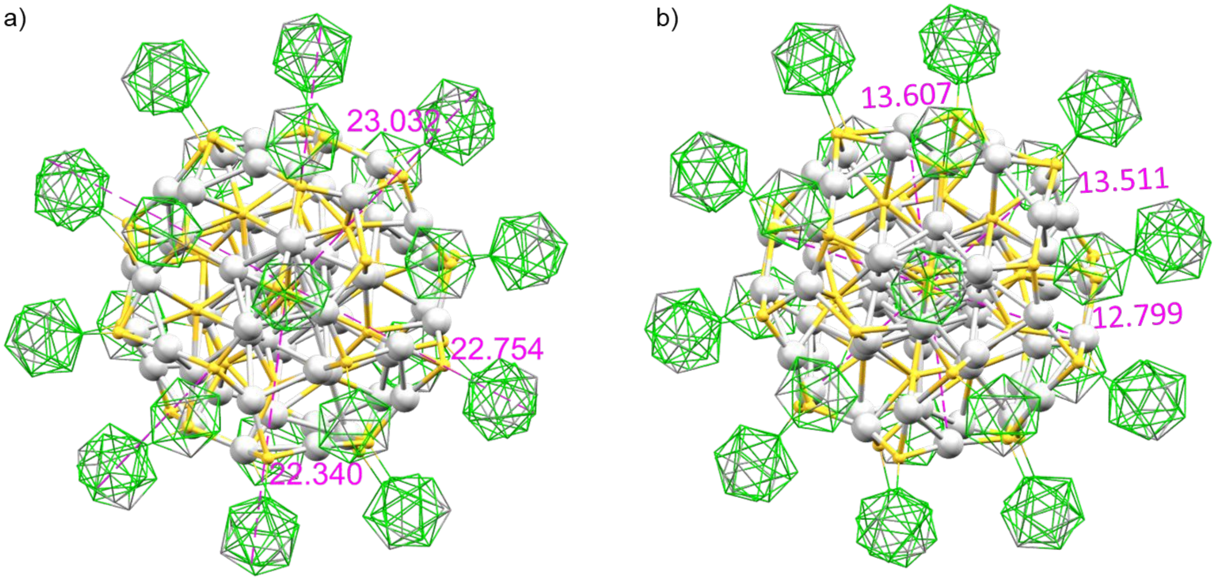

Figure S28. a) Marked distances (in Å) between the two antipodal carborane units of the cluster. b) Interatomic distances of oppositely arranged Ag atoms of the Ag–S kernel region of the cluster. Hydrogen atoms are removed for clarity.

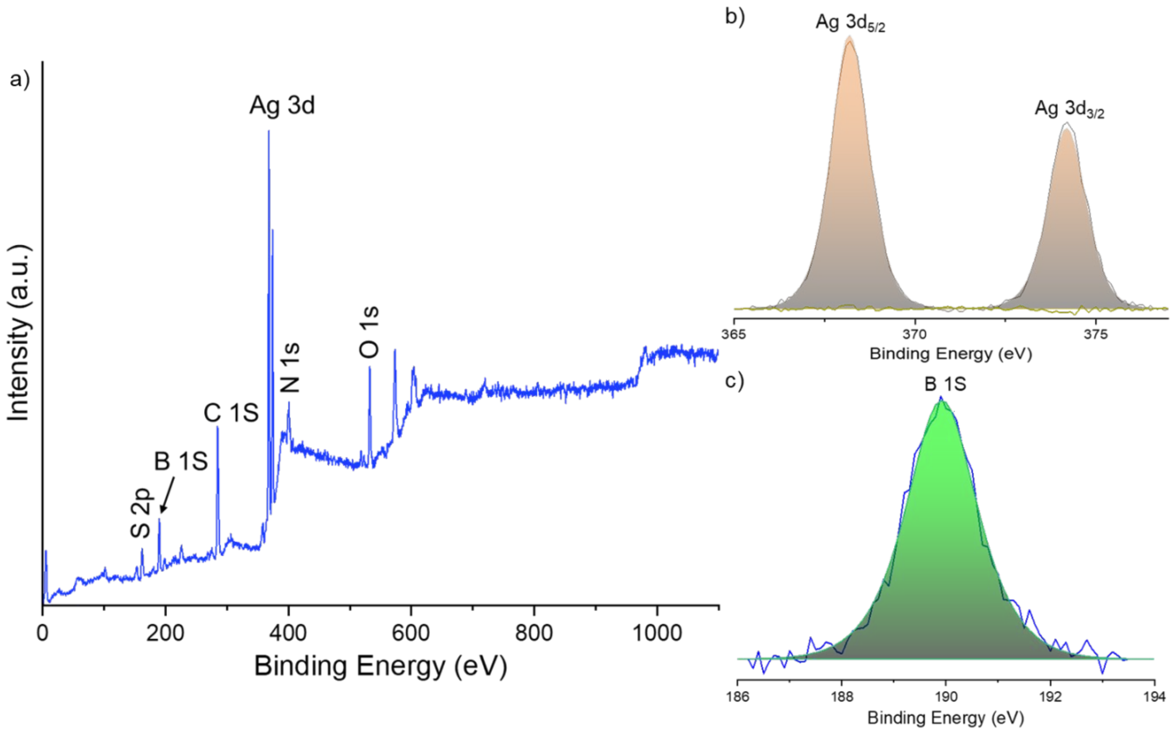

Figure S29. a) The XPS survey spectrum of Ag_{62} crystals. Selected spectral scan of b) Ag 3d and d) B 1s region of the Ag_{62} nanocluster.

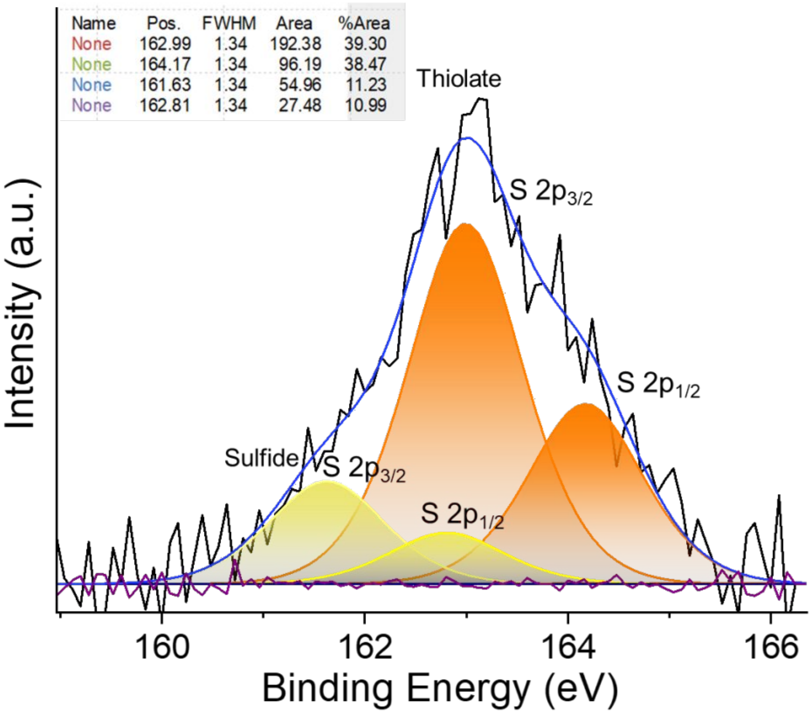

Name	Pos.	FWHM	Area	%Area
None	162.99	1.34	192.38	39.30
None	164.17	1.34	96.19	38.47
None	161.63	1.34	54.96	11.23
None	162.81	1.34	27.48	10.99

Figure S30. The XPS spectral fitting of the S 2p region of Ag_{62} nanocluster, obtained from few single crystals. Relative percentage of two types of S are shown in the inset.

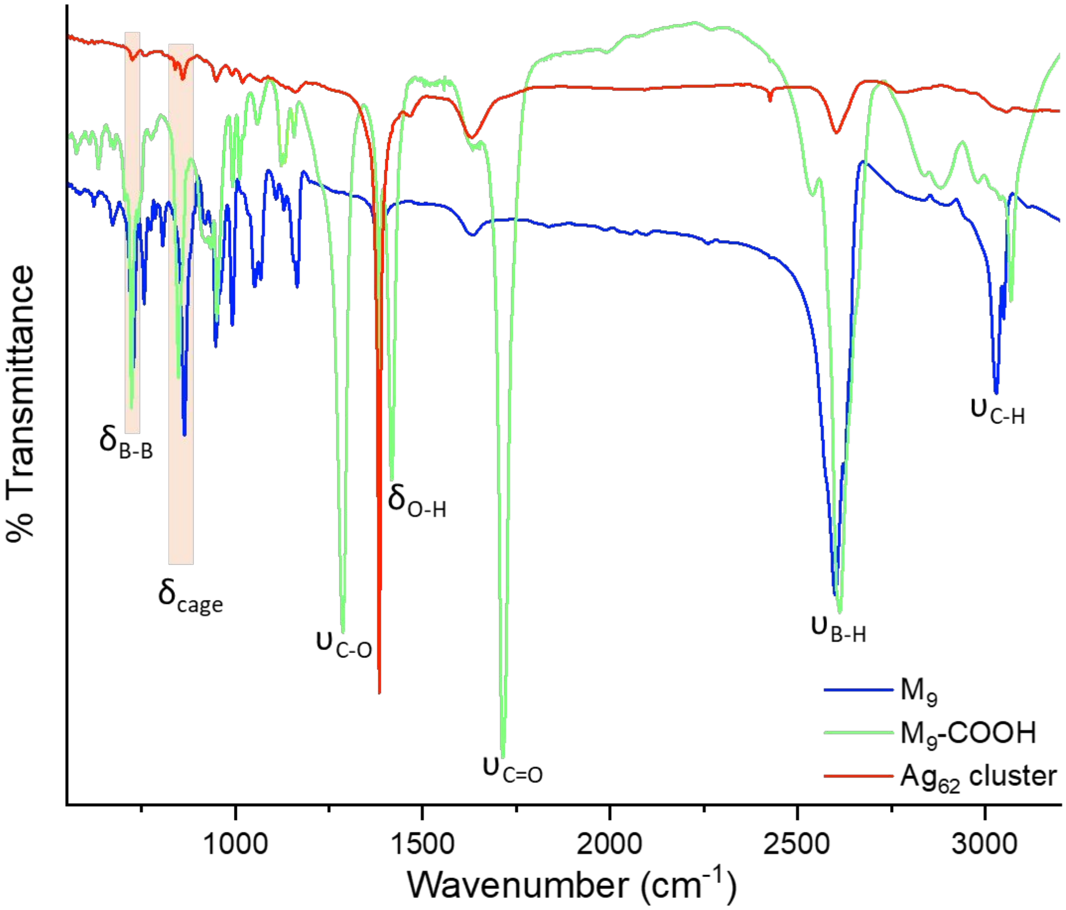

Figure S31. Comparative FT-IR spectra of M_9, M_9-COOH and Ag_{62} nanocluster. A considerable reduction in the intensity of the vibrational band was noted for the Ag_{62} nanocluster. The strong band at 1383 cm^{-1} is due to antisymmetric N–O stretching band of NO_3^- counter ions.

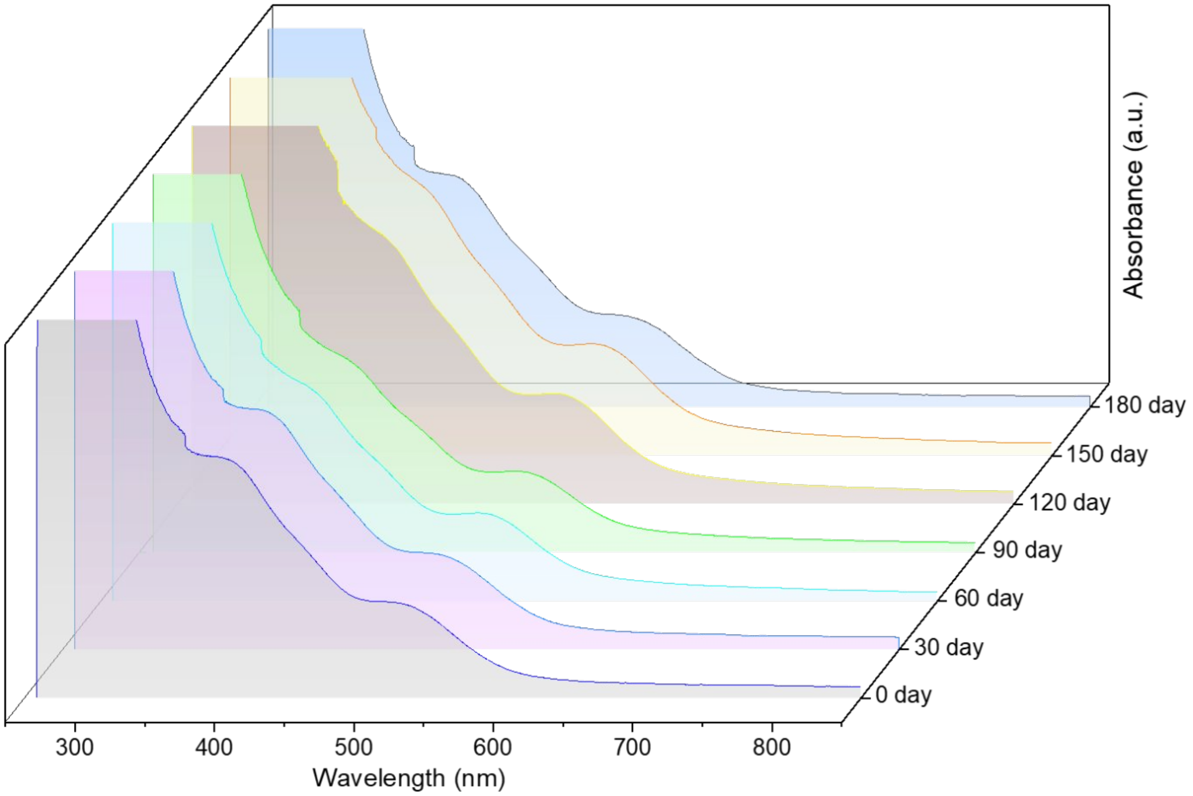

Figure S32. Time-dependent UV-vis absorption spectra of the Ag_{62} nanocluster manifested the cluster remains stable for more than 180 days under ambient condition.

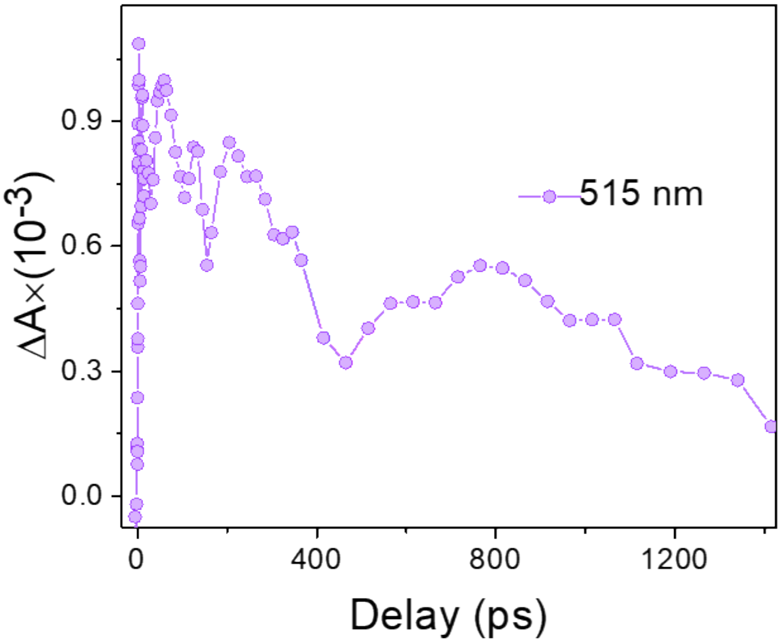

Figure S33. Kinetic decay traces for 515 nm GSPB under 400 nm pump excitation and fluence of 200 μJ.cm^{-2}.

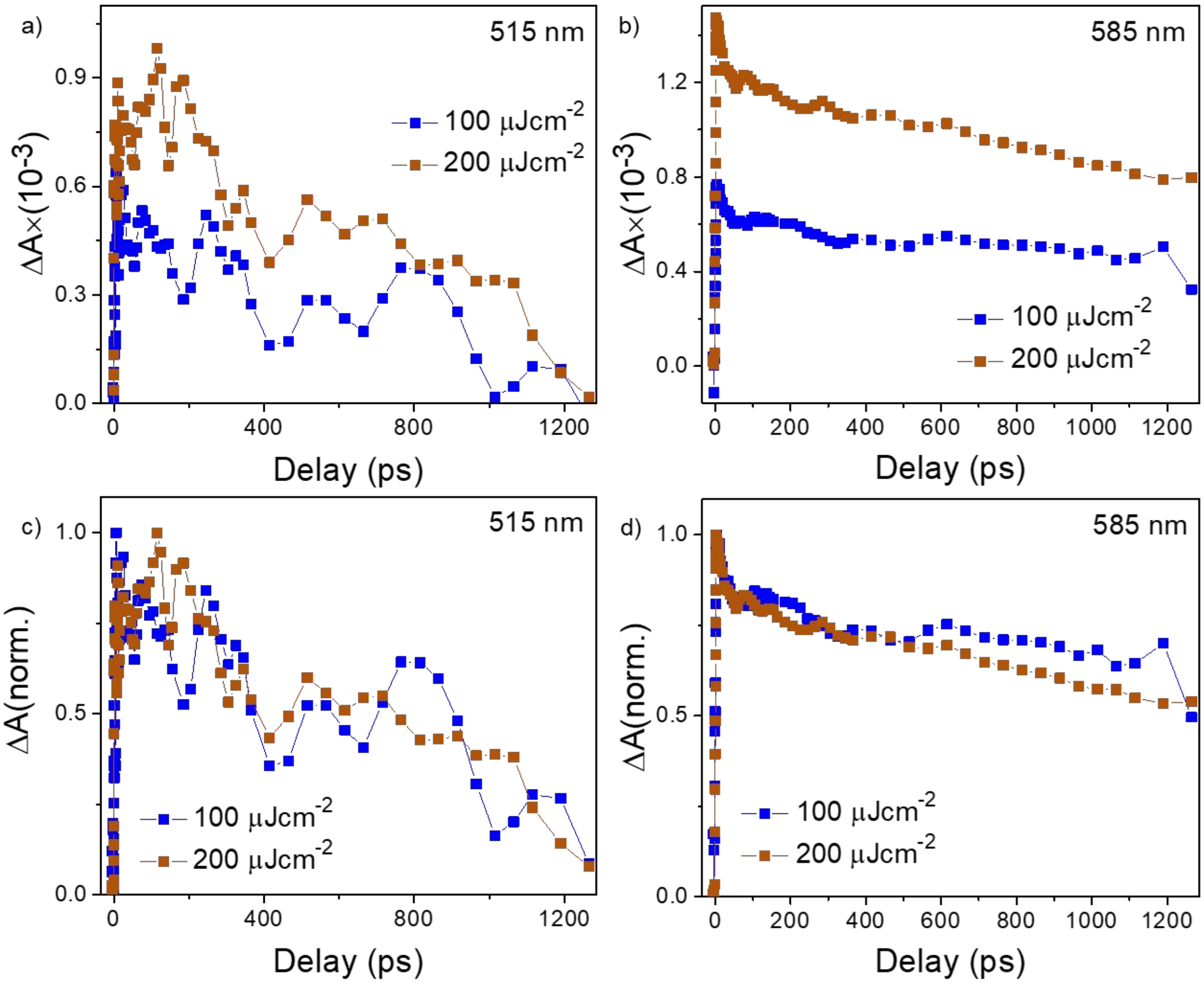

Figure S34. Pump fluence dependent comparative decay kinetics of a) 515 nm GSPB and b) 585 nm ESA peak with absolute intensity. Normalized decay kinetics for c) 515 nm GSPB and d) 585 nm ESA feature.

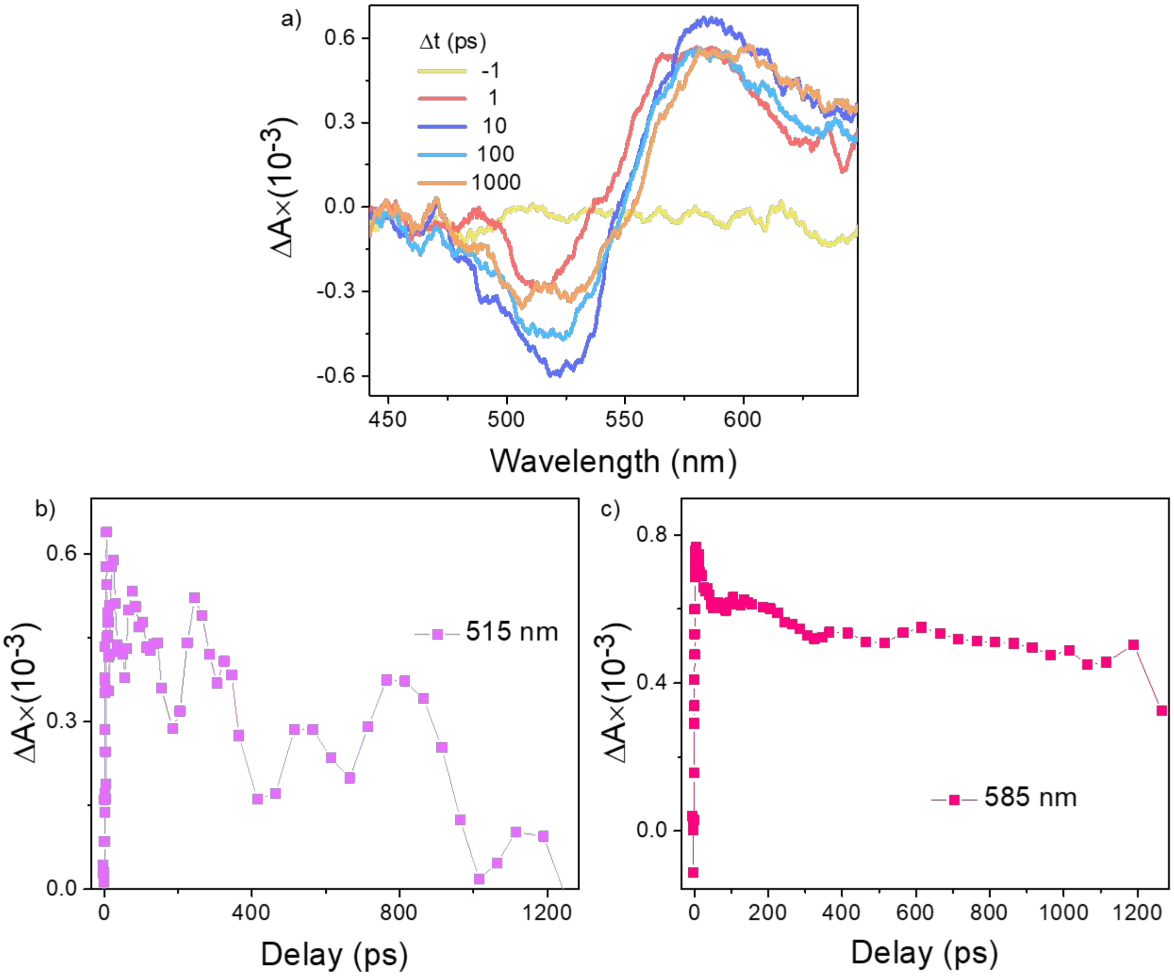

Figure S35. a) TA spectral profile of the Ag_{62} nanocluster in DMF solution under a pump excitation of 400 nm and a fluence of 100 μJ.cm^{-2} during different time evolution intervals. Kinetic decay traces of b) 515 nm GSPB and c) 585 nm ESA spectral regions.

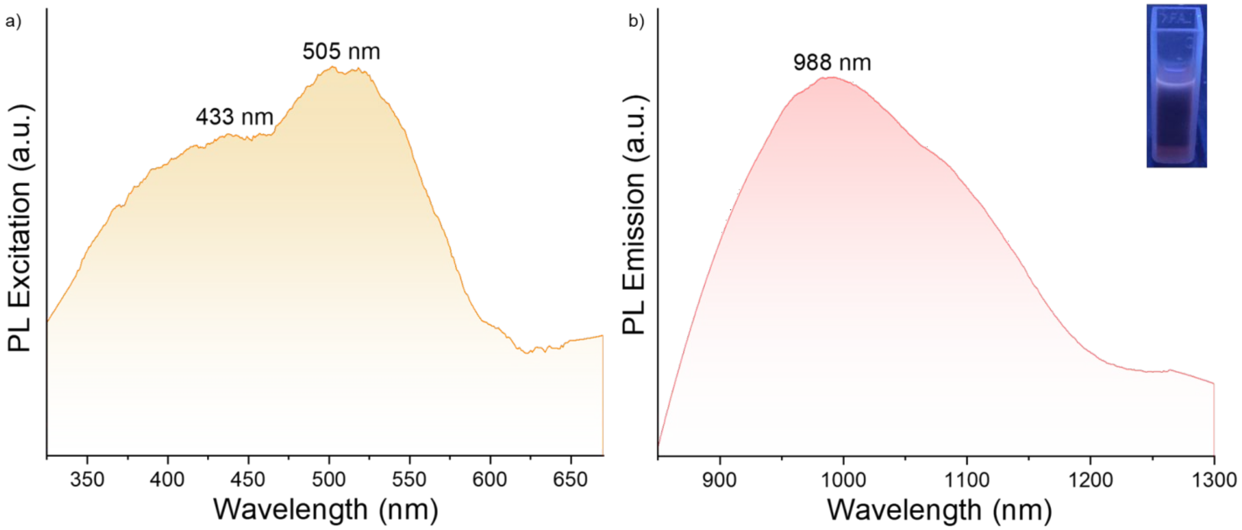

Figure S36. PL a) excitation and b) emission spectra of the Ag_{62} cluster (in DMF solution) showed a weak NIR emission band center at 988 nm having an excitation band at 505 nm and 433 nm. Inset shows the photograph of the cluster solution under 365 nm UV lamp.

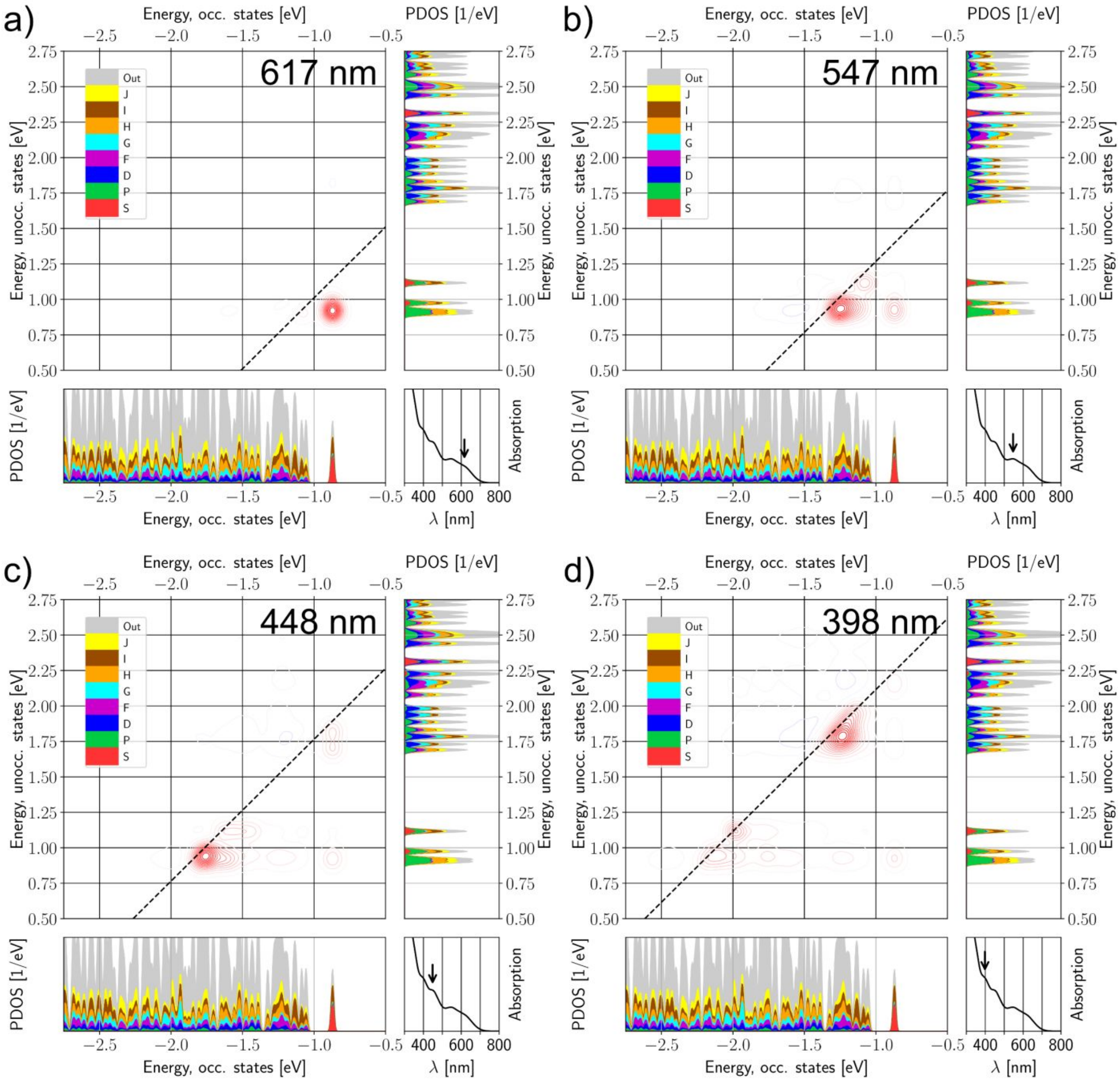

Figure S37. Dipole transition contribution map (DTCM) of the selected absorption peaks in panel. Upper left plot of each panel in a-d) shows the strengthening and screening contributions in red and blue contours respectively. Lower left and upper right plots show the projected density of states of the occupied and unoccupied Kohn-Sham states with respect to spherical harmonics functions. Lower right plot of each subfigure shows the absorption spectrum and the arrow labels the analysed feature. Different colors denote different angular momenta of the superatom state characteristics.

References:

(1) Palatinus, L.; Chapuis, G. SUPERFLIP - A Computer Program for the Solution of Crystal Structures by Charge Flipping in Arbitrary Dimensions. *J. Appl. Crystallogr.* **2007**, *40* (4), 786–790.

(2) Petříček, V.; Palatinus, L.; Plášil, J.; Dušek, M. JANA 2020 - a New Version of the Crystallographic Computing System JANA. *Zeitschrift fur Krist. - Cryst. Mater.* **2023**, *238* (7–8), 271–282.

(3) Mortensen, J. J.; Larsen, A. H.; Kuisma, M.; Ivanov, A. V.; Taghizadeh, A.; Peterson, A.; Haldar, A.; Dohn, A. O.; Schäfer, C.; Jónsson, E. Ö.; Hermes, E. D.; Nilsson, F. A.; Kastlunger, G.; Levi, G.; Jónsson, H.; Häkkinen, H.; Fojt, J.; Kangsabanik, J.; Sødequist, J.; Lehtomäki, J.; Heske, J.; Enkovaara, J.; Winther, K. T.; Dulak, M.; Melander, M. M.; Ovesen, M.; Louhivuori, M.; Walter, M.; Gjerding, M.; Lopez-Acevedo, O.; Erhart, P.; Warmbier, R.; Würdemann, R.; Kaappa, S.; Latini, S.; Boland, T. M.; Bligaard, T.; Skovhus, T.; Susi, T.; Maxson, T.; Rossi, T.; Chen, X.; Schmerwitz, Y. L. A.; Schiøtz, J.; Olsen, T.; Jacobsen, K. W.; Thygesen, K. S. GPAW: An Open Python Package for Electronic Structure Calculations. *J. Chem. Phys.* **2024**, *160* (9).

(4) Enkovaara, J.; Rostgaard, C.; Mortensen, J. J.; Chen, J.; Dułak, M.; Ferrighi, L.; Gavnholt, J.; Glinsvad, C.; Haikola, V.; Hansen, H. A.; Kristoffersen, H. H.; Kuisma, M.; Larsen, A. H.; Lehtovaara, L.; Ljungberg, M.; Lopez-Acevedo, O.; Moses, P. G.; Ojanen, J.; Olsen, T.; Petzold, V.; Romero, N. A.; Stausholm-Møller, J.; Strange, M.; Tritsaris, G. A.; Vanin, M.; Walter, M.; Hammer, B.; Häkkinen, H.; Madsen, G. K. H.; Nieminen, R. M.; Nørskov, J. K.; Puska, M.; Rantala, T. T.; Schiøtz, J.; Thygesen, K. S.; Jacobsen, K. W. Electronic Structure Calculations with GPAW: A Real-Space Implementation of the Projector Augmented-Wave Method. *J. Phys. Condens. Matter* **2010**, *22* (25).

(5) Perdew, J. P.; Burke, K.; Ernzerhof, M. Generalized Gradient Approximation Made Simple. *Phys. Rev. Lett.* **1996**, *77* (18), 3865–3868.

(6) Kuisma, M.; Ojanen, J.; Enkovaara, J.; Rantala, T. T. Kohn-Sham Potential with Discontinuity for Band Gap Materials. *Phys. Rev. B - Condens. Matter Mater. Phys.* **2010**, *82* (115106), 1–7.

(7) Walter, M.; Akola, J.; Lopez-Acevedo, O.; Jadzinsky, P. D.; Calero, G.; Ackerson, C. J.; Whetten, R. L.; Grönbeck, H.; Häkkinen, H. A Unified View of Ligand-Protected Gold Clusters as Superatom Complexes. *Proc. Natl. Acad. Sci. U. S. A.* **2008**, *105* (27), 9157–9162.

(8) Walter, M.; Häkkinen, H.; Lehtovaara, L.; Puska, M.; Enkovaara, J.; Rostgaard, C.; Mortensen, J. J. Time-Dependent Density-Functional Theory in the Projector Augmented-Wave Method. *J. Chem. Phys.* **2008**, *128* (244101), 1–10.

(9) Malola, S.; Lehtovaara, L.; Enkovaara, J.; Häkkinen, H. Birth of the Localized Surface Plasmon Resonance in Monolayer-Protected Gold Nanoclusters. *ACS Nano* **2013**, *7* (11), 10263–10270.

(10) Wang, Z. Y.; Wang, M. Q.; Li, Y. L.; Luo, P.; Jia, T. T.; Huang, R. W.; Zang, S. Q.; Mak, T. C. W. Atomically Precise Site-Specific Tailoring and Directional Assembly of

Superatomic Silver Nanoclusters. *J. Am. Chem. Soc.* **2018**, *140* (3), 1069–1076.

(11) Jana, A.; Jash, M.; Poonia, A. K.; Paramasivam, G.; Islam, M. R.; Chakraborty, P.; Antharjanam, S.; Machacek, J.; Ghosh, S.; Adarsh, K. N. V. D.; Base, T.; Pradeep, T. Light-Activated Intercluster Conversion of an Atomically Precise Silver Nanocluster. *ACS Nano* **2021**, *15* (10), 15781–15793.

(12) Wang, Q. Y.; Wang, J.; Wang, S.; Wang, Z. Y.; Cao, M.; He, C. L.; Yang, J. Q.; Zang, S. Q.; Mak, T. C. W. O-Carborane-Based and Atomically Precise Metal Clusters as Hypergolic Materials. *J. Am. Chem. Soc.* **2020**, *142* (28), 12010–12014.

(13) Li, Y. L.; Wang, J.; Luo, P.; Ma, X. H.; Dong, X. Y.; Wang, Z. Y.; Du, C. X.; Zang, S. Q.; Mak, T. C. W. Cu_{14} Cluster with Partial Cu(0) Character: Difference in Electronic Structure from Isostructural Silver Analog. *Adv. Sci.* **2019**, *6* (1900833), 1–6.

(14) Jana, A.; Duary, S.; Das, A.; Kini, A. R.; Acharya, S.; Machacek, J.; Pathak, B.; Base, T.; Pradeep, T. Multicolor Photoluminescence of Cu_{14} Clusters Modulated Using Surface Ligands. *Chem. Sci.* **2024**, *15* (34), 13741–13752.

(15) Huang, J. H.; Liu, Y. J.; Si, Y.; Cui, Y.; Dong, X. Y.; Zang, S. Q. Carborane-Cluster-Wrapped Copper Cluster with Cyclodextrin-like Cavities for Chiral Recognition. *J. Am. Chem. Soc.* **2024**, *146* (24), 16729–16736.

(16) Huang, J. H.; Liu, L. Y.; Wang, Z. Y.; Zang, S. Q.; Mak, T. C. W. Modular Cocrystallization of Customized Carboranylthiolate-Protected Copper Nanoclusters via Host-Guest Interactions. *ACS Nano* **2022**, *16* (11), 18789–18794.

(17) Li, Y. L.; Wang, Z. Y.; Ma, X. H.; Luo, P.; Du, C. X.; Zang, S. Q. Distinct Photophysical Properties in Atom-Precise Silver and Copper Nanocluster Analogues. *Nanoscale* **2019**, *11* (12), 5151–5157.

(18) Jana, A.; Unnikrishnan, P. M.; Poonia, A. K.; Roy, J.; Jash, M.; Paramasivam, G.; Machacek, J.; Adarsh, K. N. V. D.; Base, T.; Pradeep, T. Carboranethiol-Protected Propeller-Shaped Photoresponsive Silver Nanomolecule. *Inorg. Chem.* **2022**, *61* (23), 8593–8603.

(19) Wang, J.; Wang, Z. Y.; Li, S. J.; Zang, S. Q.; Mak, T. C. W. Carboranealkynyl-Protected Gold Nanoclusters: Size Conversion and UV/Vis–NIR Optical Properties. *Angew. Chemie - Int. Ed.* **2021**, *60* (11), 5959–5964.

(20) Wang, J.; Xu, F.; Wang, Z. Y.; Zang, S. Q.; Mak, T. C. W. Ligand-Shell Engineering of a Au_{28} Nanocluster Boosts Electrocatalytic CO_2 Reduction. *Angew. Chemie - Int. Ed.* **2022**, *61* (32), 1–6.

(21) Huang, J. H.; Wang, Z. Y.; Zang, S. Q.; Mak, T. C. W. Spontaneous Resolution of Chiral Multi-Thiolate-Protected Ag_{30} Nanoclusters. *ACS Cent. Sci.* **2020**, *6* (11), 1971–1976.

(22) Huang, J. H.; Si, Y.; Dong, X. Y.; Wang, Z. Y.; Liu, L. Y.; Zang, S. Q.; Mak, T. C. W. Symmetry Breaking of Atomically Precise Fullerene-like Metal Nanoclusters. *J. Am. Chem. Soc.* **2021**, *143* (32), 12439–12444.

(23) Jana, A.; Jash, M.; Dar, W. A.; Roy, J.; Chakraborty, P.; Paramasivam, G.; Lebedkin, S.;

Kirakci, K.; Manna, S.; Antharjanam, S.; Machacek, J.; Kucerakova, M.; Ghosh, S.; Lang, K.; Kappes, M. M.; Base, T.; Pradeep, T. Carborane-Thiol Protected Copper Nanoclusters: Stimuli-Responsive Materials with Tunable Phosphorescence. *Chem. Sci.* **2022**, *14* (6), 1613–1626.

(24) Wang, J.; Cai, J.; Ren, K. X.; Liu, L.; Zheng, S. J.; Wang, Z. Y.; Zang, S. Q. Stepwise Structural Evolution toward Robust Carboranealkynyl-Protected Copper Nanocluster Catalysts for Nitrate Electroreduction. *Sci. Adv.* **2024**, *10* (18), 1–8.

(25) Yadav, V.; Jana, A.; Acharya, S.; Malola, S.; Nagar, H.; Sharma, A.; Kini, A. R.; Antharjanam, S.; Machacek, J.; Nair, K.; Devi, V.; Base, T.; Häkkinen, H.; Pradeep, T. Site-Specific Substitution in Atomically Precise Carboranethiol-Protected Nanoclusters and Concomitant Changes in Electronic Properties. *Nat. Commun.* **2025**, *16* (1197), 1–13.